J. Fluid Mech. (2014), *vol.* 757, *pp.* 908–942.
doi:10.1017/jfm.2014.504

Disorganization of a hole tone feedback loop by an axisymmetric obstacle on a downstream end plate

K. Matsuura[1,†] **and M. Nakano**[2]

[1]Graduate School of Science and Engineering, Ehime University, 3 Bunkyo-cho, Matsuyama, Ehime 790-8577, Japan

[2]Institute of Fluid Science, Tohoku University, 2-1-1 Katahira, Aoba-ku, Sendai, Miyagi 980-8577, Japan

(Received 19 August 2013; revised 30 July 2014; accepted 27 August 2014; first published online 29 September 2014)

This study investigates the suppression of the sound produced when a jet, issued from a circular nozzle or hole in a plate, goes through a similar hole in a second plate. The sound, known as a hole tone, is encountered in many practical engineering situations. The mean velocity of the air jet u_0 was 6–12 m s^{-1}. The nozzle and the end plate hole both had a diameter of 51 mm, and the impingement length L_{im} between the nozzle and the end plate was 50–90 mm. We propose a novel passive control method of suppressing the tone with an axisymmetric obstacle on the end plate. We find that the effect of the obstacle is well described by the combination (W/L_{im}, h) where W is the distance from the edge of the end plate hole to the inner wall of the obstacle, and h is the obstacle height. The tone is suppressed when backflows from the obstacle affect the jet shear layers near the nozzle exit. We do a direct sound computation for a typical case where the tone is successfully suppressed. Axisymmetric uniformity observed in the uncontrolled case is broken almost completely in the controlled case. The destruction is maintained by the process in which three-dimensional vortices in the jet shear layers convect downstream, interact with the obstacle and recursively disturb the jet flow from the nozzle exit. While regions near the edge of the end plate hole are responsible for producing the sound in the controlled case as well as in the uncontrolled case, acoustic power in the controlled case is much lower than in the uncontrolled case because of the disorganized state.

Key words: absolute/convective instability, aeroacoustics, jets

1. Introduction

The sound produced when a jet, issued from a circular nozzle or hole in a plate, goes through a second plate that has a hole of the same diameter is referred to as a hole tone. The hole tone is a fluid dynamic self-excited oscillation where axisymmetric coherent vortices are produced in the naturally unstable jets, convected downstream, and the generation and feedback of induced disturbances occur from some points in

† Email address for correspondence: matsuura.kazuo.mm@ehime-u.ac.jp

the flow near the surface on which the vortices are impinging (Rayleigh 1945; Blake 1986; Howe 1998; Ginevsky, Vlasov & Karavosov 2010). Jet tone phenomena that are similar to the hole tone and involve impinging surfaces include the edge and ring tones (Rockwell & Naudascher 1979; Blake 1986; Ginevsky *et al.* 2010). The interaction of the jet shear layer and the surface gives rise to strong self-excited oscillations with frequencies determined by the flow speed, the initial thickness of the mixing layer, and the distance from the nozzle edge to the downstream obstacle (Ginevsky *et al.* 2010). Past research on the hole tone was summarized in the introduction of Matsuura & Nakano (2012). Practically, we encounter the tone in many systems such as solid propellant rocket motors, automobile intakes and exhaust systems, ventilation systems, gas distribution systems, and whistling kettles. It often becomes a source of unfavourable sound and vibration. The present study investigates the suppression of the tone.

Rayleigh (1945), on the basis of his observations, conjectured on the original hole tone mechanism, now known as a feedback mechanism (Rayleigh 1945; Rossiter 1962; Chanaud & Powell 1965; Rockwell & Naudascher 1979). This mechanism is considered to consist of four elements, i.e. the birth of disturbances in the jet shear layer, the convection and amplification of the disturbances leading to the formation of vortices, the generation of pressure waves due to vortex impingement, and the upstream propagation of pressure waves that initiates the disturbances by means of a receptivity process. In the mechanism, as a result of the axisymmetric instabilities of the jet, each vortex is convected over the impingement length, i.e. the gap, L_{im} during a time of the order of L_{im}/u_c, at the shear-layer convection velocity u_c that is typically about half the mean jet speed at the nozzle exit u_0. An impulsive disturbance is generated when the vortex impinges on the downstream edge, which initiates the formation of a new vortex in the shear layer. The impulse takes a finite time $\sim L_{im}/c_\infty$ to travel back across the gap, where c_∞ is the speed of sound. Based on this picture, the frequency f of the vortex formation satisfies $n/f \sim L_{im}/u_c + L_{im}/c_\infty$, where the values $n = 1, 2, 3$, etc. correspond to the various stages of operation (Rossiter 1962). Matsuura & Nakano (2012) conducted direct computations of a hole tone feedback system at Mach numbers around 0.029. They found two regions of large contribution to instantaneous acoustic power. The region of the largest contribution is the outer edge of a separation region near the upstream edge of the end plate hole. The second is the upstream side of the end plate near the hole edge. The former is considered to be the major sound source of the pressure waves propagating inside the jet, whereas the latter is considered to be the major sound source of the pressure waves propagating outside the jet. Considering these results, they proposed an axisymmetric throttling mechanism linking mass flow rates through the end plate hole, vortex impingement and global pressure propagation. Although understanding of aeroacoustic dynamics of the hole tone has developed considerably, control methods with which to suppress the tone have been scarcely reported.

The suppression of the hole tone appears to result in the interception of the cycle of the feedback. When we think back to the hole tone mechanism, the interception of the feedback corresponds to artificially altering at least one of the four elements mentioned above. Ginevsky *et al.* (2010) reported two suppression methods for self-excited oscillations due to jet impingement on a baffle. One is to reduce the azimuthal homogeneity of jet mixing layers near a nozzle by introduction of three cones, which causes weak attenuation of coherent structures. The other is to disrupt the jet coherent structures at the point of their collision with the baffle. The two methods are related to the first and third elements. Langthjem & Nakano (2010)

conducted a numerical simulation of the hole tone feedback cycle based on a three-dimensional discrete vortex method. Evaluation of the sound generated by the self-sustained flow oscillations was based on the Powell–Howe theory of vortex sound and a boundary integral/element method. They investigated the effects of imposing non-axisymmetric perturbations of the jet on sound reduction including both standing and travelling (rotating) waves. The method is related to the first element mentioned above.

More generally, much attention has been paid to control for suppressing flow-induced oscillation because of its fundamental interest and practical applications (Cattafesta *et al.* 2003; Rowley & Williams 2006; Ginevsky *et al.* 2010; Izawa 2011). Roughly speaking, strategies are categorized into passive and active control (Gad-el-Hak 2000). Passive control does not need a power supply, and has the advantage that the control system is simpler than an active control system, which requires actuators. Possible examples of the passive control of fluid dynamic oscillation are disturbing flows by making vortices irregular with a tripping wire, serration or chevron nozzle, stabilizing unstable flows with a plate, planing off corners to weaken pressure pulses or remove the cause of oscillation, and changing the Reynolds number. Although there are such possibilities, the applicability and limitations of passive control are not well established for the hole tone. Therefore, this study focuses on the passive control of the hole tone.

We propose a brand-new passive control method for the hole tone using an axisymmetric obstacle on the end plate that is different from the above methods. The obstacle is used to block and return upstream, as a turbulent flow, the fluid flowing in the radial direction along the end plate, which is a portion of the jet that did not flow out of the end plate hole after vortex impingement.

In § 2, we explain the strategy of the passive control we propose, and experimental details such as the experimental apparatus, proposed obstacle shapes for suppressing the hole tone, and experimental conditions. In § 3, we present experimental results for various obstacle sizes, air-jet velocities and impingement lengths. By these, we show that overall effect of the obstacles on suppressing the hole tone can be summarized in terms of the two parameters W/L_{im} and h, where W is the distance from the edge of the end plate hole to the inner wall of the obstacle, and h is the obstacle height. We also show the effect of changing the obstacle height on the velocity profile of the jet shear layer, the effect of changing the impingement length on the velocity profile, and flow structures where the hole tone is or is not successfully suppressed. In § 4, we explain the numerical analysis conducted in the following section. In § 5, we perform a direct sound computation to clarify the effect of the obstacle on vortical structures and instantaneous acoustic power. In § 6, we draw conclusions from this study.

2. Experimental system

First, we explain the strategy of the passive control of the hole tone we propose in figure 1. Figure 1(*a*) shows the feedback loop of the baseline hole tone. As mentioned in the introduction, the feedback phenomena are considered to consist of four elements. These elements occur in phase to maintain the feedback loop. We explain the present control strategy in figure 1(*b*). It efficiently disorganizes the feedback loop by disturbing the birth and growth of organized vortical structures in jet shear layers using flows dammed up and reversed by the obstacle, which originally escape in the radial direction from entering the end plate hole after vortex impingement.

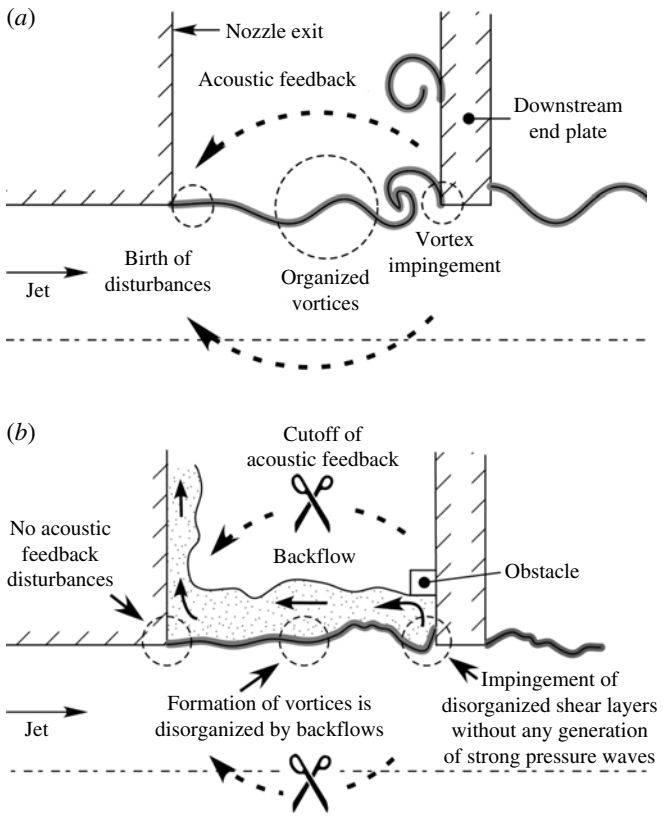

FIGURE 1. Explanation of the present passive control strategy of the hole tone. (*a*) Baseline hole tone feedback loop. (*b*) Disorganization of the feedback loop.

Figure 2 shows the experimental system with the proposed obstacle for the passive control of the hole tone. The nozzle plate and the downstream end plate are rectangular, with dimensions of 300 mm × 300 mm and 270 mm × 200 mm, respectively. The hole and end plate are acoustically compact. The diameters of the nozzle and end plate hole are both $d_0 = 51$ mm. The thickness of the end plate is 10 mm. The impingement length L_{im} is the variable distance between the nozzle exit and the end plate. The ring obstacle is attached to the end plate, as shown in figure 2. The inner radius, outer radius and height of the obstacle are denoted as r_i, r_e and h, respectively. Here, the difference $r_e - r_i$ is kept at 5 mm. The distance from the upstream edge of the end plate hole to the inner wall of the obstacle is defined as $W \equiv r_i - d_0/2$. We vary r_i, h, L_{im} and u_0. Table 1 gives the obstacle sizes (r_i, h), impingement lengths L_{im}, and air-jet mean velocities u_0 tested for each setting (r_i, h, L_{im}). The obstacles are grouped into eight types depending on r_i. Types A, B, C, D, E, F, G and H correspond to $r_i = 25.5$, 30.5, 33.0, 35.5, 38.0, 40.5, 43.0 and 45.5 mm, respectively. We vary h for each type, and vary L_{im} using the end plate with each obstacle of (r_i, h). Then, we vary u_0 for each combination of (r_i, h, L_{im}). The table also shows the important configuration parameter W/L_{im}.

Air from a centrifugal blower goes through an approximately 160 mm long mouthpiece before leaving the nozzle. When the end plate is removed, the ratios of the half-width to the momentum thickness (Michalke 1984) in the shear layers

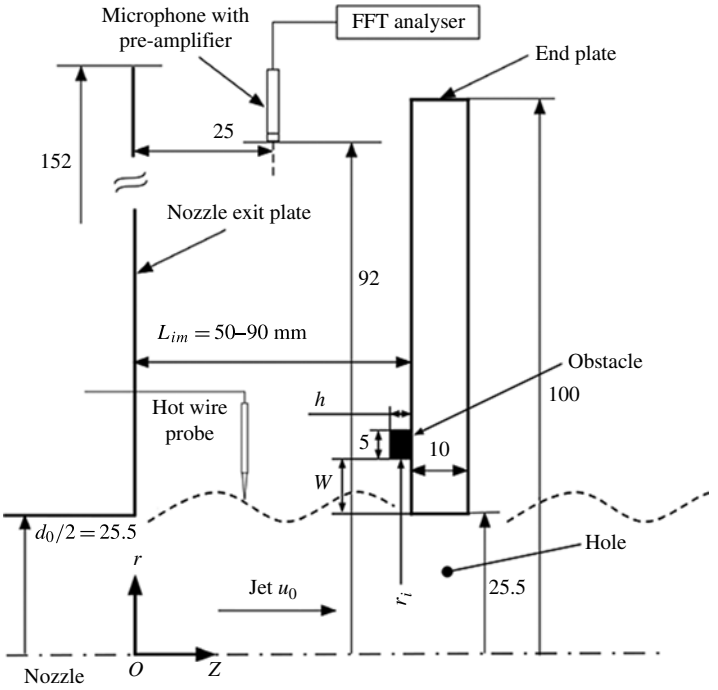

FIGURE 2. Experimental system. Dimensions are in mm.

of the jet issuing from the nozzle exit are $R_h/\delta_\theta = 48.8$, 25.5, 14.2 and 17.5 for $u_0 = 6$, 8, 10 and 12 m s^{-1}, respectively. Here, R_h is the jet half-width such that a streamwise velocity $u_z(R_h) = u_0/2$ and δ_θ is the momentum thickness at the nozzle exit. The shape factors of the boundary layers just upstream of the nozzle exit when the end plate is removed are 2.41, 2.40, 2.36 and 2.35 for $u_0 = 6$, 8, 10 and 12 m s^{-1}, respectively, and the boundary layer states at the nozzle exit are laminar for all the jet velocities. Shear layer profiles are measured by an I-type hot wire. The sampling rate of the hot wire is 5 kHz. It has been established that the insertion of the hot wire does not influence the hole-tone frequency and amplitude. The intensity of the free-stream disturbance at the nozzle exit when the end plate is removed is approximately 1.2–1.5 % for the above jet velocities.

The jet velocities have inevitable uncertainties due to changes in the experimental environment, including its thermal non-equilibrium, although we calibrated our wind tunnel for each run and tried to keep the room temperature at 20 °C with an air conditioner. Accepting the uncertainties, we regard the jet velocities in the range from 9.5 to 10.4 m s^{-1} as 10 m s^{-1}. Sound pressure (SP) is measured at $r = 92$ mm by a condenser microphone as shown in figure 2. The signal is passed through a microphone preamplifier to a fast Fourier transform (FFT) analyser. The sampling rate of the microphone is 2.56 kHz. We obtained a spectrum from 2048 sampled data points by FFT. We performed 20 times of ensemble average to obtain a final spectrum. The microphone is located sufficiently away from the centreline and does not affect jet flows. To take instantaneous snapshots of the jet shear layers, a laser sheet is used with a high-speed video camera with the smoke of evaporated glycol solvent injected into the jets. The thickness of the laser sheet is approximately 1 mm. The sampling rate of the snapshots is 1500 frames s^{-1}. It has been established that

Type	r_i (mm)	h (mm)	L_{im} (mm)	W/L_{im}	u_0 (m s^{-1})
A	25.5	2, 5	50	0.000	10
B	30.5	2, 3, 5, 8	50	0.100	10
C	33.0	2, 3, 4, 8	50	0.150	10
			60	0.125	
			70	0.107	
			80	0.094	
			90	0.083	
D	35.5	2, 3, 5	50	0.200	6, 8, 10, 12
		2.5, 8	50	0.200	10
		2, 2.5, 3, 5, 8	60	0.167	10
			70	0.143	
			80	0.125	
			90	0.111	
E	38.0	3	50	0.250	10
F	40.5	2, 3, 4, 6, 8	50	0.300	10
			60	0.250	
			70	0.214	
			80	0.188	
			90	0.167	
G	43.0	3, 4, 5, 6, 7	50	0.350	10
			60	0.292	
			70	0.250	
			80	0.219	
			90	0.194	
H	45.5	4, 5, 6, 7, 8	50	0.400	10
			60	0.333	
			70	0.286	
			80	0.250	
			90	0.222	

TABLE 1. Obstacle size (r_i, h), impingement length L_{im}, and air-jet velocities u_0 tested for each system setting (r_i, h, L_{im}); $W \equiv r_i - d_0/2$.

the sheet goes through the centre of the hole. The smoke is injected at the air intake of the centrifugal blower so that the injection does not disturb the jet.

3. Experimental results

3.1. *Characteristics of tone suppression by an obstacle in terms of the sound pressure spectrum*

On the basis of the SP spectrum, we study the effect of changing the obstacle size on suppressing the hole tone when $u_0 = 10$ m s^{-1} and $L_{im} = 50$ mm. Figure 3 shows the measured SP spectra for types A, B, D, and H. The results of changing h are shown for each type. 'Baseline' in the legend means the baseline hole tone without any obstacle on the end plate. When type A is used with $h = 2$ and 5 mm, peaks around the frequency f_0 of the baseline hole tone still appear with only slight shifts in frequency. The SP spectra for both heights are narrowband, similar to the baseline

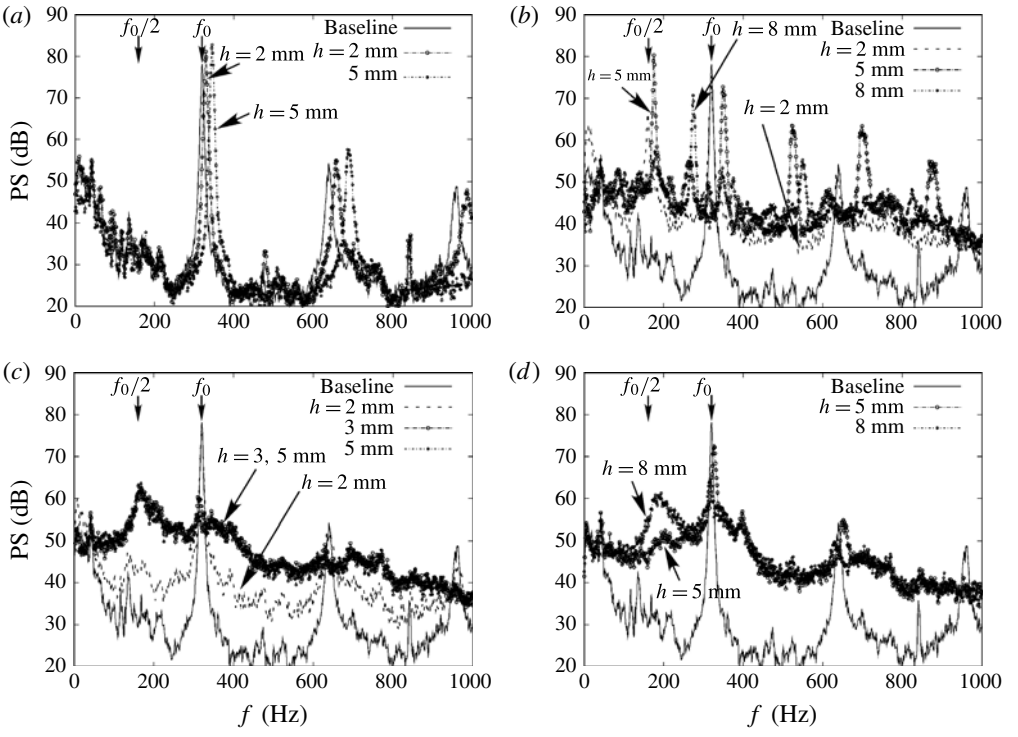

FIGURE 3. Effect of obstacle size on the hole tone suppression when $u_0 = 10$ m s^{-1} and $L_{im} = 50$ mm: (*a*) Type A ($r_i = 25.5$ mm), (*b*) type B ($r_i = 30.5$ mm), (*c*) type D ($r_i = 35.5$ mm), (*d*) type H ($r_i = 45.5$ mm).

case, indicating that the feedback loop with organized vortices remains unchanged in the flow fields. This is also understood from the visualization of flow structures shown later in figure 11(*a*). Therefore, type A obstacles of both heights are not effective in suppressing the tone. Roughly speaking, adding an obstacle with $W = 0$ is equivalent to reducing L_{im} from the standpoint of shear-layer impingement on the inner corner. According to the simple relation for the feedback loop between the tone frequency f and L_{im} which was mentioned in the introduction, f is inversely proportional to L_{im}. So, the frequency shift without change of overall spectral shape is expected, with a tone at higher frequency when the obstacle is installed with respect to the baseline. When type B with $h = 2$ mm is used, peaks appear around f_0 and the subharmonic frequency $f_0/2$. The levels of the power spectrum (PS) for broadband frequencies other than f_0 and $f_0/2$ also increase. When $h = 5$ mm, the peak around $f_0/2$ becomes higher than that around f_0. As found from the shifts in peak frequencies, type B succeeds in affecting the jet shear layer. However, an unwanted strong peak around $f_0/2$ appears when $h = 5$ mm. When $h = 8$ mm, the peak around $f_0/2$ decreases with a slight shift of the original f_0 peak to a lower frequency. The maximum PS is reduced by 13 dB compared with the baseline case. When type D is used, the peak at f_0 remains unchanged when $h = 2$ mm. However, when $h \geqslant 3$ mm, the SP spectra become broadband and the peak at f_0 almost vanishes. A new peak appears at $f_0/2$. The maximum peak around $f_0/2$ is approximately 15 dB lower than that around f_0 for the baseline hole tone. The SP spectrum for $h = 5$ mm is almost identical to that for

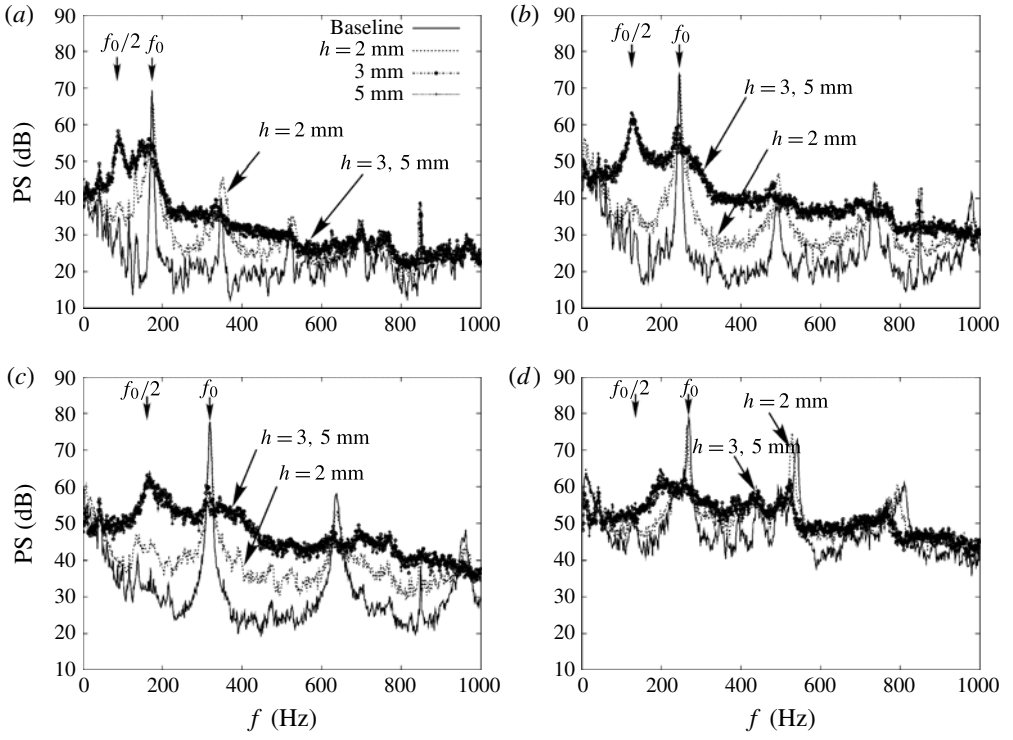

FIGURE 4. Effect of the jet speed u_0 on the hole tone suppression for obstacle type D ($r_i = 35.5$ mm) when $L_{im} = 50$ mm: (*a*) $u_0 = 6$ m s^{-1}, (*b*) $u_0 = 8$ m s^{-1}, (*c*) $u_0 = 10$ m s^{-1}, (*d*) $u_0 = 12$ m s^{-1}.

$h = 3$ mm, and the tone suppression effect therefore become saturated. When type H is used, the SP spectrum becomes broadband compared with the baseline hole tone, but the peak around f_0 remains unchanged when $h = 5$ mm. When $h = 8$ mm, the magnitudes of the peaks at $f_0/2$ and f_0, which are approximately 15 dB lower than the peak of the baseline hole tone, are almost the same. When we define an effective obstacle as one that reduces the maximum PS of the baseline case by 10 dB, type B with $h = 8$ mm, type D with $h = 3$ and 5 mm, and type H with $h = 8$ mm are judged as effective when $L_{im} = 50$ mm and $u_0 = 10$ mm. Common features in these cases are the appearance of a peak at $f_0/2$ and an increase in the PS of broadband frequencies other than f_0 and $f_0/2$. They correspond to an interaction between the corner vortex and the jet coming from the nozzle exit, which we call the main jet, and the appearance of turbulence. The former is explained in § 5.4, and the latter is understood from the visualization of flow structures shown later in figure 11.

Next, we study the effect of changing u_0 on suppressing the hole tone for type D with $L_{im} = 50$ mm. Figure 4 shows the measured SP spectra for $u_0 = 6$, 8, 10 and 12 m s^{-1}. The results of changing h are shown for each case. When $h = 2$ mm, the PS for broadband frequencies other than f_0 increase a little overall for all u_0. The peak at f_0 is unaffected. When $h \geqslant 3$ mm, the original peak is remarkably reduced. Peaks that are not observed in the baseline hole tone appear at low frequencies close to $f_0/2$ except for $u_0 = 12$ m s^{-1}. While the PS at these frequencies become the most dominant, the tone is considerably reduced for all u_0. Therefore, the obstacle is effective in suppressing the tone, irrespective of the values of u_0 considered here.

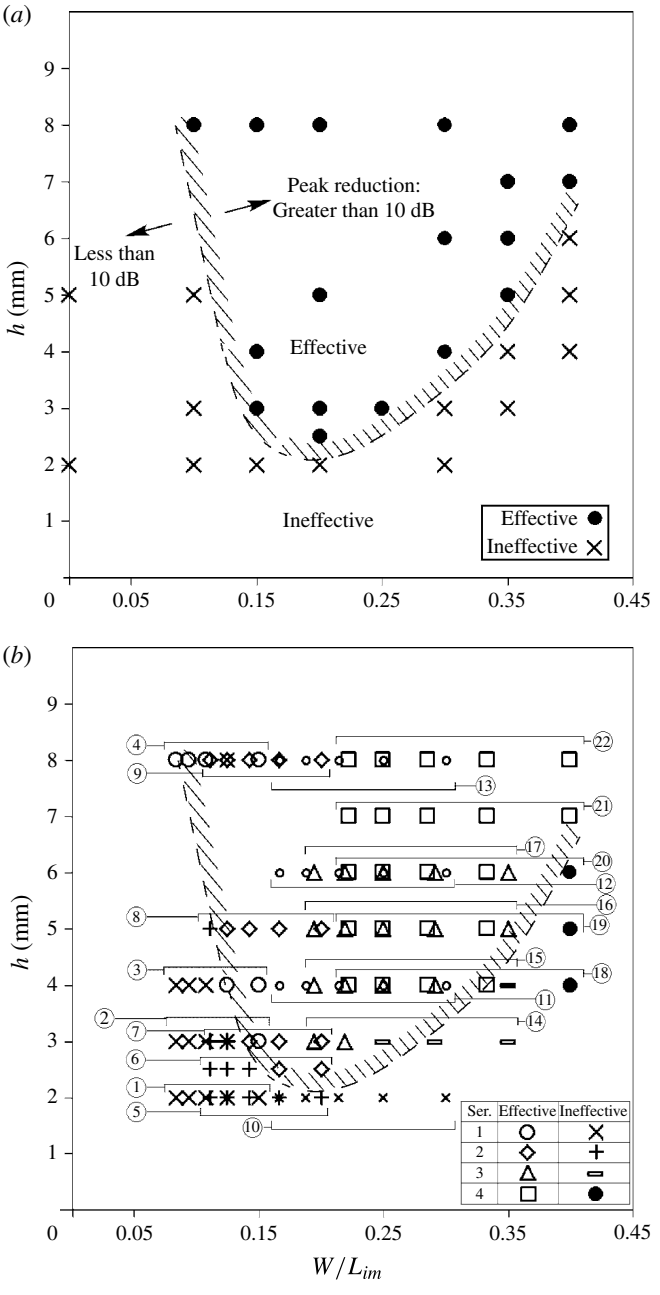

FIGURE 5. Effective and ineffective obstacles in suppressing the hole tone when $u_0 = 10$ m s^{-1}. (*a*) Effective and ineffective obstacles when $L_{im} = 50$ mm. (*b*) Change between effective cases and ineffective cases when L_{im} is varied (the size of the symbols is changed to separate different series where they overlap.)

3.2. *Overall effect of the obstacles on suppressing the hole tone when* $u_0 = 10$ m s^{-1}

Following the above discussion on the characteristics of tone suppression by an obstacle in terms of the SP spectrum, figure 5 shows the effect on suppressing the hole tone for a wide range of system settings (r_i, h, L_{im}) when $u_0 = 10$ m s^{-1}. The data

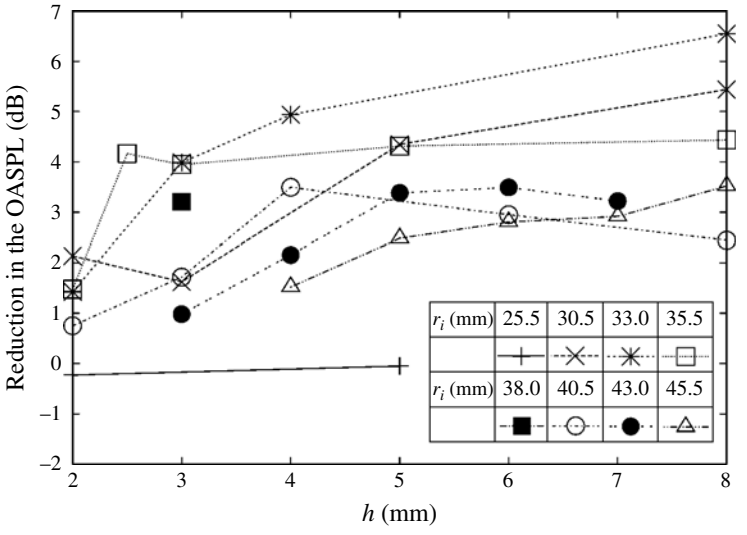

FIGURE 6. Reductions in overall SPL of the frequency range below 2 kHz compared with the baseline case when $L_{im} = 50$ mm and $u_0 = 10$ m s^{-1}.

are summarized by the two parameters W/L_{im} and h. Figure 5(*a*) shows effective and ineffective obstacles when $L_{im} = 50$ mm and $u_0 = 10$ m s^{-1}. Here we use the definition of an effective obstacle proposed in § 3.1 and draw a curve of the border between the effective and ineffective obstacles. The effective region has a tongue-like shape with the effective point of the minimum $h \sim 2.5$ mm around $W/L_{im} = 0.2$. Figure 5(*b*) shows changes between effective cases and ineffective cases when L_{im} is varied for $u_0 = 10$ m s^{-1}. We tested 22 obstacle sizes of $r_i = 33$, 33.5, 40.5, 43 and 45.5 mm for L_{im} of 50–90 mm. We call a trace of varying L_{im} on the plot between W/L_{im} and h for each obstacle size a 'series'. Within a series, changes between effective and ineffective cases are observed definitely when the series crosses the border introduced previously between the effective and ineffective cases, as confirmed by the series ②, ③, ⑥, ⑦, ⑧, ⑮, ⑱, ⑲ and ⑳. This evidence strongly supports the use of the parameters W/L_{im} and h, and the validity of the curve separating the effective and ineffective cases on the plot of the parameters. On the other hand, strictly speaking, there are exceptions because the criterion of 10 dB is arbitrarily set. Peaks around $f_0/2$ do not become large as L_{im} increases in series ④, and high peaks remain at f_0 even if L_{im} increases in series ⑭ near the bottom of the effective region, although the results are not shown here.

Figure 6 shows reductions in the overall SP level (OASPL) of the frequency range below 2 kHz compared with the baseline case when $L_{im} = 50$ mm and $u_0 = 10$ m s^{-1}. Larger suppression effects approximately of 4–6 dB for $h = 3$–8 mm are observed for 30.5 mm $\leqslant r_i \leqslant$ 35.5 mm than for r_i larger than 40.5 mm. Except for type A, effects of tone suppression are observed. Generally, the reduction in the overall sound pressure level increases as h increases. Also, the effects of increasing h when h is small are larger than those when h is large as found from the comparison of data around $h = 2$ and 5 mm. It might seem that the reduction of 4–6 dB mentioned above is small. Because broadband components increase while the discrete, i.e. peak, components are reduced, reductions in the OASPL appear to be modest. However, because the noisy peak component is greatly reduced, sound quality changes drastically.

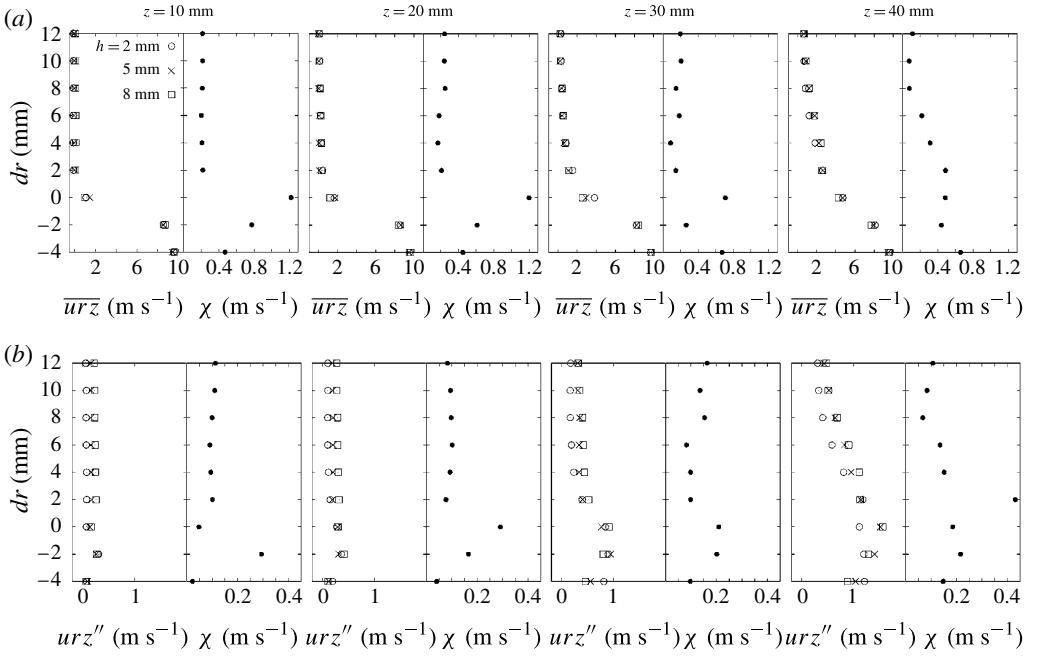

FIGURE 7. Effect of the obstacle height on the velocity profiles of the jet shear layers when $u_0 = 10$ m s^{-1} for obstacle type B with $L_{im} = 50$ mm where $dr \equiv r - d_0/2$ and $urz \equiv \sqrt{u_r^2 + u_z^2}$. (*a*) Mean velocity profile $\overline{urz}$ and its half-uncertainties χ. (*b*) Profiles of the r.m.s. of velocity fluctuation urz'' and its half-uncertainties χ.

3.3. *Effect of the system setting on the velocity profiles of jet shear layers*

Figures 7 and 8 show the effect of changing h on the velocity profiles of the jet shear layers and associated data uncertainties when $u_0 = 10$ m s^{-1} and $L_{im} = 50$ mm for types B and D. The profiles of the mean velocity and the root-mean-square (r.m.s.) of the velocity fluctuations with the uncertainties are shown at $z = 10$, 20, 30 and 40 mm. Measurements are conducted three times to evaluate a velocity profile for each obstacle size. We change h on two different paths in figure 5(*a*). One is a path for $W/L_{im} = 0.1$ using type B with $h = 2$, 5 and 8 mm. The cases of $h = 2$ and 5 mm lie in the ineffective region, while the case of $h = 8$ mm lies in the effective region. The other is a path for $W/L_{im} = 0.2$ using type D with $h = 2$, 3 and 5 mm. The case of $h = 2$ mm lies in the ineffective region, while the cases of $h = 3$ and 5 mm lie in the effective region. Figures 7(*a*) and 8(*a*) have two abscissae. One is the time average of $\sqrt{u_r^2 + u_z^2}$, where u_r and u_z are the instantaneous velocity components in the r and z directions, respectively. We denote the averaged velocity as $\overline{urz}$. The other is the maximum of half of the 90 % confidence intervals χ of $\overline{urz}$ among $h = 2$, 5 and 8 mm, i.e.

$$\chi \equiv \max_{h \in (2,5,8)} \left\{ t_{N_{max}-1} \frac{\sigma}{\sqrt{N_{max}}} \right\}. \tag{3.1}$$

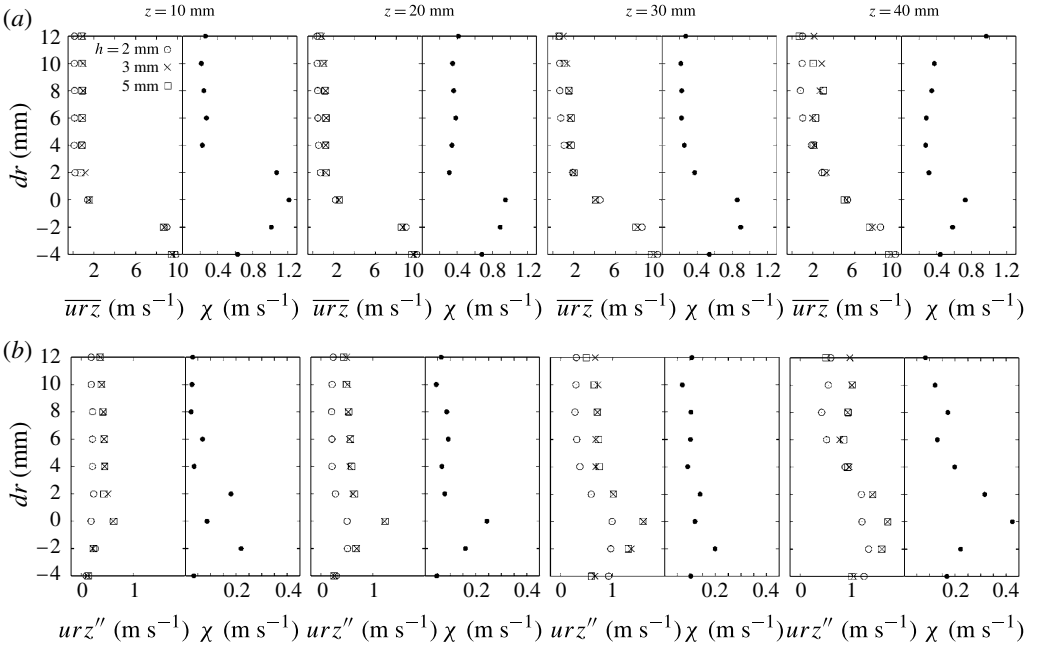

FIGURE 8. Effect of the obstacle height on the velocity profiles of the jet shear layers when $u_0 = 10$ m s^{-1} for type D with $L_{im} = 50$ mm where $dr \equiv r - d_0/2$ and $urz \equiv \sqrt{u_r^2 + u_z^2}$. (*a*) Mean velocity profile $\overline{urz}$ and its half-uncertainties χ. (*b*) Profiles of the r.m.s. of velocity fluctuation urz'' and its half-uncertainties χ.

Here, by assuming x_i as a single experimental datum of $\overline{urz}$

$$N_{max} = 3, \quad \bar{x} \equiv \frac{1}{N_{max}} \sum_{i=1}^{N_{max}} x_i, \quad \sigma \equiv \sqrt{\frac{1}{N_{max} - 1} \sum_{i=1}^{N_{max}} (x_i - \bar{x})^2}, \tag{3.2a–c}$$

and $t_{N_{max}-1} = 2.920$ for Student's t-distribution (Student 1908).

Similarly, figures 7(*b*) and 8(*b*) also have two abscissae. One is the r.m.s. of the velocity fluctuations $urz'' \equiv urz - \overline{urz}$. The other is the maximum half of the 90 % confidence intervals of urz'' among $h = 2, 5$ and 8 mm evaluated similarly to the case of $\overline{urz}$ and denoted also as χ. In figures 7 and 8, the ordinate is $dr \equiv r - (d_0/2)$.

For type B with $L_{im} = 50$ mm, the effect of changing h is generally small except for $z = 40$ mm, which is consistent with the fact that the jet shear layers are not so much affected, and consequently, the path fully lies in the ineffective region. However, for type D with $L_{im} = 50$ mm, large differences between $h = 2$ and 3 mm are observed in profiles of both $\overline{urz}$ and urz'', which is consistent with the fact that $h = 2$ mm is ineffective and $h = 3$ mm is effective. The differences are evident not only at $z = 40$ mm but also at $z = 10$ mm, which means that backflows from the obstacle, which are also found in figure 11 shown later, strongly affect the nozzle exit, where disturbances begin to grow in the jet shear layers, when $h \geqslant 3$ mm. The results for $h = 3$ and 5 mm are almost the same, which is consistent with figure 3(*c*). This fact means that a region near the interior corner of the obstacle determines the strength of backflows.

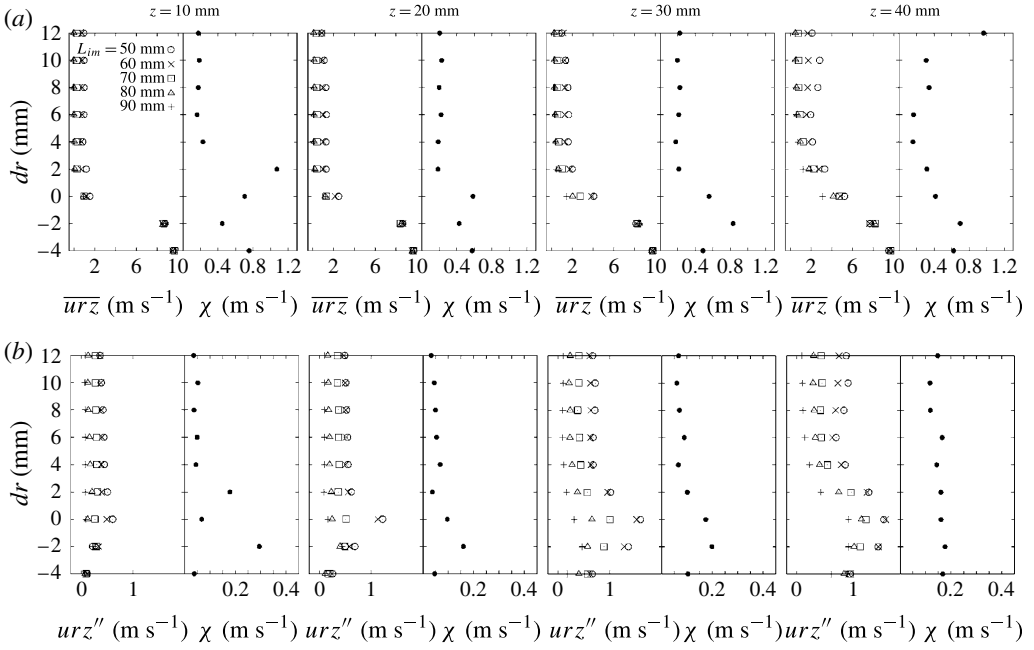

FIGURE 9. Effect of the impingement length L_{im} on the velocity profiles of the jet shear layers when $u_0 = 10$ m s^{-1} for type D with $h = 3$ mm where $dr \equiv r - d_0/2$ and $urz \equiv \sqrt{u_r^2 + u_z^2}$. (*a*) Mean velocity profile $\overline{urz}$ and its half-uncertainties χ. (*b*) Profiles of the r.m.s. of velocity fluctuation urz'' and its half-uncertainties χ.

Figures 9 and 10 show the effect of changing L_{im} with fixed h on the velocity profiles of the jet shear layers when $u_0 = 10$ m s^{-1}. L_{im} is varied on two different paths. One path is $(W, h) = (10$ mm, 3 mm), i.e. type D, with $L_{im} = 50$, 60, 70, 80 and 90 mm corresponding to $W/L_{im} = 0.20$, 0.166, 0.142, 0.125 and 0.111. The path corresponds to series ⑦ in figure 5(*b*). The first three cases are effective, and the others are ineffective. The other path is $(W, h) = (15$ mm, 4 mm), i.e. type F, with $L_{im} = 50$, 60, 70, 80 and 90 mm corresponding to $W/L_{im} = 0.30$, 0.250, 0.214, 0.187 and 0.166. The path corresponds to series ⑪ in the figure. This path lies fully in the effective region.

When $L_{im} = 50$ and 60 mm for type D with $h = 3$ mm, $\overline{urz}$ and urz'' for $dr > 0$ are non-zero, which means that backflows from the obstacle affect the nozzle exit. As L_{im} increases, $\overline{urz}$ and urz'' for $dr > 0$ approach zero at $z = 10$ and 20 mm. Therefore, influences of the backflows from the obstacle on the nozzle exit vanish as L_{im} increases, which is consistent with the fact that $L_{im} = 80$ and 90 mm belong to the ineffective region. In the case of type F with $h = 4$ mm, $\overline{urz}$ and urz'' do not approach zero and the velocity profiles remain almost the same, which means that backflows from the obstacle continue to affect the nozzle exit even if L_{im} increases. This is because the inner diameter of type F is larger than that of type D, and consequently backflows reach further upstream. This trend is consistent with the fact that this case lies fully in the effective region.

Summarizing the above discussion, figures 7–10 show that the nozzle exit regions are strongly affected by backflows from the obstacles in the effective cases. In figure 5(*a*), we separated the obstacles into effective and ineffective based on the

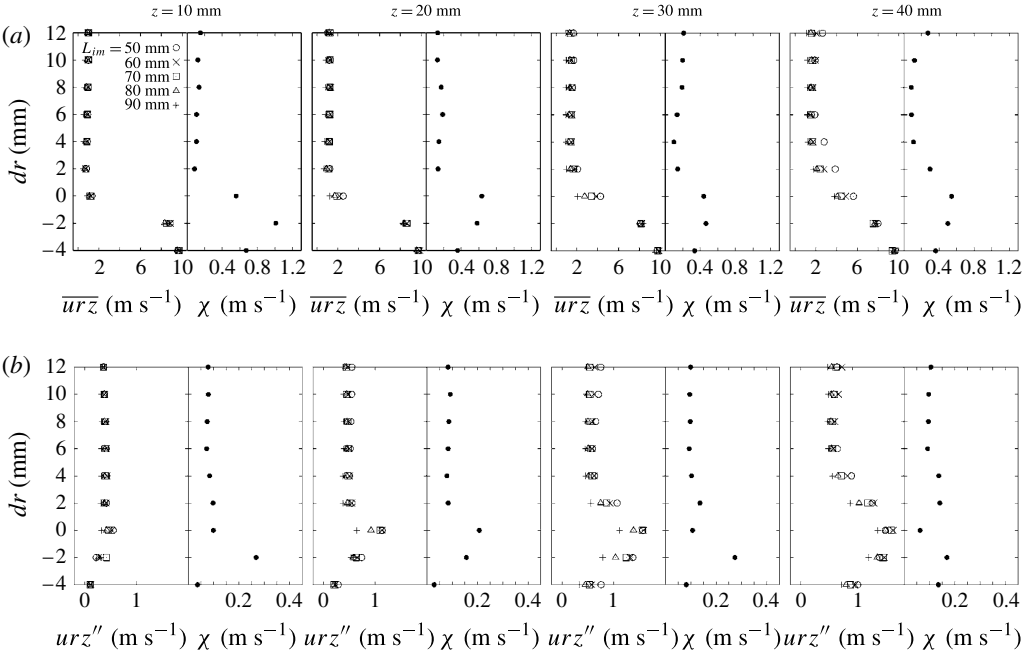

FIGURE 10. Effect of the impingement length on the velocity profiles of the jet shear layers when $u_0 = 10$ m s^{-1} for type F with $h = 4$ mm where $dr \equiv r - d_0/2$ and $urz \equiv \sqrt{u_r^2 + u_z^2}$. (*a*) Mean velocity profile $\overline{urz}$ and its half-uncertainties χ. (*b*) Profiles of the r.m.s. of velocity fluctuation urz'' and its half-uncertainties χ.

definition proposed in § 3.1. When we compare urz'' at $z = 10$ mm in parts (*b*) of figures 7–10, urz'' at $dr \sim 2$ mm, i.e. near the jet shear layers of the nozzle exit, is larger than approximately 0.4 m s^{-1} in all the effective cases: thus urz'', which shows the influence of backflows, of 0.4 m s^{-1} appears to be another threshold for the separation of obstacles.

3.4. *Flow structures when the hole tone is successfully suppressed*

Figure 11(*a–f*) shows flow structures for various obstacle shapes when $u_0 = 10$ m s^{-1} and $L_{im} = 50$ mm. Schematic flow structures are shown in addition to the experimental snapshots of the flow structures obtained with the laser-smoke method. Figures 11(*a*), 11(*c*) and 11(*e*) are ineffective cases, and 11(*b*), 11(*d*) and 11(*f*) are effective cases. In 11(*b*), 11(*d*), 11(*e*) and 11(*f*), we see vortical rotation and flow paths in the snapshots as a motion blur due to a slow shutter. In the ineffective cases, we can see regular organized vortices in the jet shear layers, which means that the regular feedback loop is maintained. In the effective cases, highly turbulent flows eject from the inner side of the obstacle, and then mix with and recursively disturb the jet from the nozzle at upstream positions sufficiently sensitive to break regular organized vortices. This is confirmed by the disordered state of the white mist. The turbulent backflows explain the broadband distribution of the PS in figures 3 and 4. The influence of the backflows is also confirmed both by the swelling of the velocity profiles near $dr = 8$ and 10 mm and by the non-zero velocities for $dr > 0$ near the nozzle exit in figure 8.

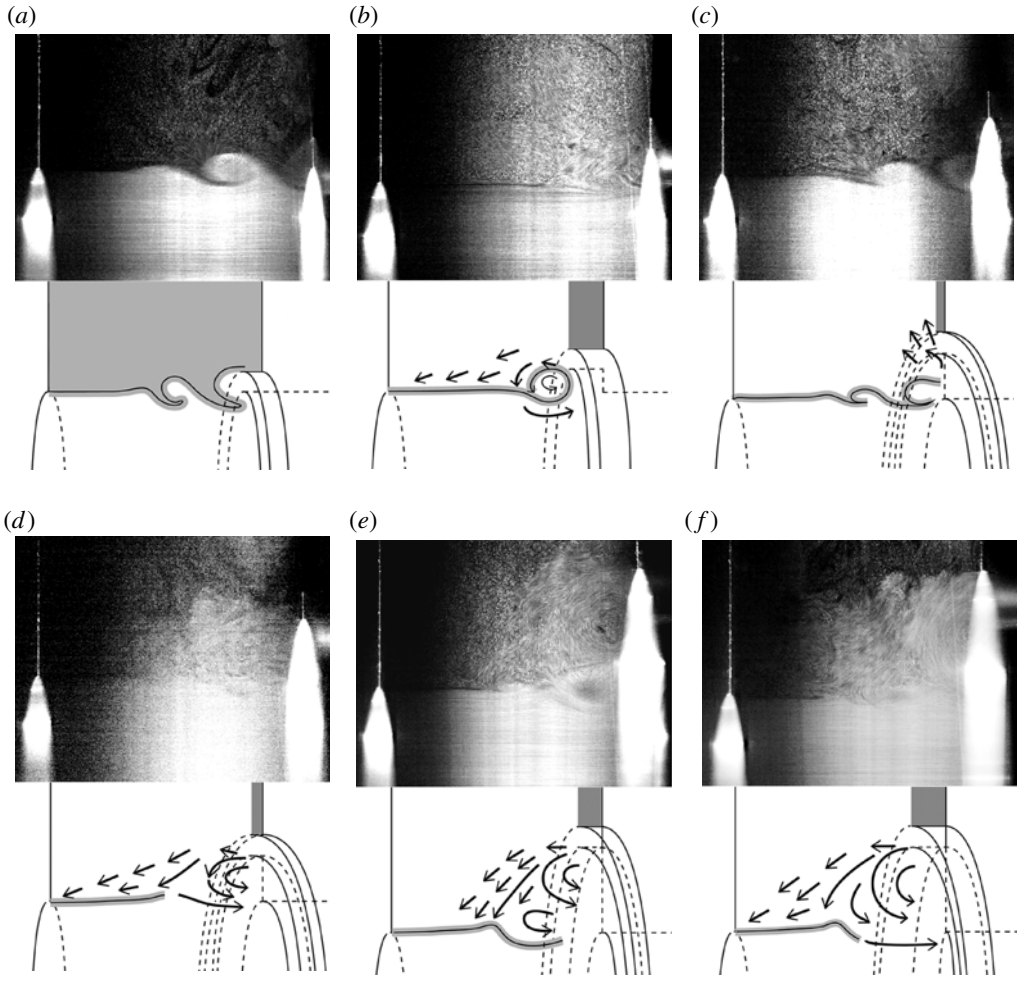

FIGURE 11. Visualization of flow structures for various obstacle shapes when $u_0 = 10$ m s^{-1} and $L_{im} = 50$ mm (upper: experimental snapshot, lower: schematic flow structure). (*a*) Type A ($r_i = 25.5$ mm), $h = 5$ mm (ineffective). (*b*) Type B ($r_i = 30.5$ mm), $h = 8$ mm (effective). (*c*) Type D ($r_i = 35.5$ mm), $h = 2$ mm (ineffective). (*d*) Type D ($r_i = 35.5$ mm), $h = 3$ mm (effective). (*e*) Type H ($r_i = 45.5$ mm), $h = 5$ mm (ineffective). (*f*) Type H ($r_i = 45.5$ mm), $h = 8$ mm (effective).

We now re-examine figure 5(*a*) considering the flow structures mentioned above. When W is small, vortices in the jet shear layers tend to collide with the obstacle. The obstacle is ineffective because recirculation with backflows, which affects the jet shear layers, is not generated. On the other hand, when W is large, vortices in the jet shear layers collide with the hole edge. Because the momentum of fluid which does not go through the end plate hole and proceeds in the radial direction becomes too small to affect the jet shear layers, the obstacle is again ineffective. The range of W in which the recirculation with backflows strongly affects the jet shear layers is between the above two limits. The division of W by L_{im} includes two effects. One is that the jets diverge as they go downstream, i.e. non-parallel effects, and the other

is that the influence of the recirculation with backflows becomes local near the end plate as L_{im} increases. The value of h indicates the degree of blockage of the radially flowing fluid.

4. Numerical analysis

In the previous section, we showed that the passive control method using the axisymmetric obstacle we propose is effective in suppressing the hole tone, and also clarified the effective combination of parameters, i.e. $(W/L_{im},\ h)$. In all the effective cases, turbulent backflows affecting the shear layers of the main jet, and the appearance of the subharmonic frequency of the baseline hole tone are observed. In order to explain the mechanism which leads to these common features, and to show the link between the features and tone suppression, we conduct a direct sound computation. Details of the present numerical method are explained in Matsuura & Nakano (2012). The governing equations are the unsteady three-dimensional fully compressible Navier–Stokes equations in general coordinates (ξ, η, ζ). The perfect gas law closes the system of equations. Sutherland's formula for viscosity is adopted and a constant Prandtl number of $Pr = 0.72$ is assumed. The equations are solved using the finite-difference method. Spatial derivatives that appear in the metrics, convective and viscous terms are evaluated using the sixth-order tridiagonal compact scheme (Lele 1992). Near boundaries, the fourth-order one-sided and classical Padé scheme is used at the boundaries and one point internal to them. Time-accurate solutions to the governing equations are obtained using the third-order explicit Runge–Kutta scheme. The time increment is constant and set at $\Delta t = 2.4 \times 10^{-4} L_{im}/c_\infty$ in all flow fields. The Courant–Friedrichs–Lewy (CFL) numbers of the present computations, which are defined by the maximum sums of a contravariant velocity and the speed of sound scaled by metrics as

$$CFL \equiv \Delta t \max\left(|U_1| + c_\infty\sqrt{\xi_{x_i}\xi_{x_i}},\ |U_2| + c_\infty\sqrt{\eta_{x_i}\eta_{x_i}},\ |U_3| + c_\infty\sqrt{\zeta_{x_i}\zeta_{x_i}}\right), \tag{4.1}$$

are around 0.4. Here, $(x, y, z) = (x_1, x_2, x_3)$ are Cartesian coordinates, U_i $(i = 1, 2, 3)$ are the contravariant velocities, ξ_i, η_i, ζ_i $(i = x, y, z)$ are the metrics. In addition to the above-mentioned spatial discretization and time integration, a tenth-order implicit filtering (Gaitonde & Visbal 2000) is introduced to suppress numerical instabilities that arise from central differencing in the compact scheme. The filter parameters that appear in the left-hand side are set to be 0.33 for $i = 2$ and $i_{max} - 1$, 0.492 for $2 < i < i_{max} - 1$. Near the boundaries, implicit filters of orders $p = (4, 4, 6, 8, 10)$ for $i = (2, \ldots, 6)$ and $i = (i_{max} - 1, \ldots, i_{max} - 5)$, are used. Here, $i \in (k, l)$, and indices j, k, l respectively run in the circumferential θ, radial r and streamwise z directions in the general coordinate system applied to the computational grid mentioned later. Periodicity in the θ direction is treated strictly without employing a one-sided biased scheme near the branch cut with regard to the derivative and filtering scheme. This O-type topology has a singularity at the centreline. To circumvent this, primitive values, circumferentially averaged at $k = 2$, are inserted into the primitive values at $k = 1$:

$$f_{j,1,l} = \frac{1}{j_{max} - 1}\sum_{i=1}^{j_{max}-1} f_{i,2,l}, \quad \forall (j, l) \in \{1, \ldots, j_{max}\} \times \{1, \ldots, l_{max}\}. \tag{4.2}$$

The present numerical method has been well validated for the prediction of transitional and turbulent subsonic flows (Matsuura & Kato 2007; Matsuura & Nakano 2012).

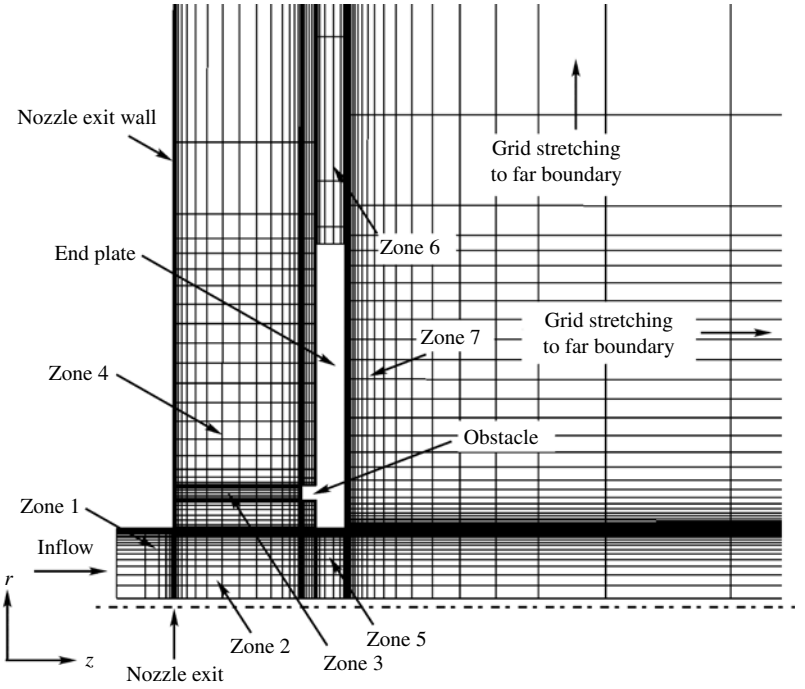

FIGURE 12. Computational grid for $\theta = 0$ rad. (Every fifth grid line in the r and z directions is drawn.)

We choose the obstacle geometry of type D, i.e. $r_i = 35.5$ mm, with $h = 5$ mm for the computation as mentioned later in § 5. The impingement length L_{im} and the air-jet velocity u_0 are 50 mm and 10 m s^{-1}, respectively. This computation assumed the standard atmospheric conditions, i.e. a temperature of 20 °C and a pressure of 1 atm as the ambient conditions. At 20 °C, $u_0 = 10$ m s^{-1} corresponds to a Reynolds number $Re = u_0 d_0/\nu = 3.39 \times 10^4$ and a Mach number $Ma = u_0/c_\infty = 0.029$, where the speed of sound $c_\infty = 343$ m s^{-1} and the kinematic viscosity $\nu = 1.51 \times 10^{-5}$ m^2 s^{-1}. Figure 12 shows an overview of the computational grid consisting of seven zones. We generate cylindrical-coordinate grids (r, θ, z) of the O-type topology in each zone. The total number of grid points is 9.07×10^6. The nozzle exit corresponds to $z = 0$ mm. Exact overlapping of five grid lines in the normal direction to an interface is used between neighbouring zones. The $z = 0$ plane outside the nozzle in figure 12 is modelled as a wall, which is consistent with a corresponding experimental system shown in figure 4 of Matsuura & Nakano (2011). The nozzle exit plate is removed in figures 15 and 17 for drawing clarity.

Mesh widths are made fine so as to capture jet shear layers accurately in the r direction, and in the separation regions near the nozzle exit, the end plate hole and the obstacle in the r and z directions. The maximum grid width Δ_{max} in the z direction between the nozzle exit and the end plate is ∼1.00 mm. The minimum grid width Δ_{min}/d_0 is 4.9×10^{-4}. Compared to the computational grids used in previous computations for the baseline hole tone (Matsuura & Nakano 2011, 2012), we only change the distribution of grid points near the obstacle.

The initial condition is an interpolated flow field onto the present grid of the baseline hole tone where self-sustained oscillation occurs. Regarding the boundary

conditions, the sponge layer method (Freund 1997) assuming inflow velocity profiles consistent with experimental data is used near the nozzle inlet, i.e. $\Omega_{z,in} = [d_0/51,\ d_0/2] \times [0,\ 2\pi) \times [-d_0/2.55,\ -d_0/10.2]$. In the baseline and obstacle cases, shear layers near the nozzle exit are perturbed by inherently generated flows. To avoid disrupting naturally oscillating structures, no excitation such as random forcing is imposed at the inlet boundary. Although some fundamental convective instability of round jets is well known (Michalke 1984), little is known at present about the effects of inlet disturbances on the hole tone and they will be investigated in the future. The regions $\Omega_{r,ex} = [7.11d_0,\ 41.7d_0] \times [0,\ 2\pi) \times [0,\ 41.4d_0]$ and $\Omega_{z,ex} = [d_0/51,\ 41.7d_0] \times [0,\ 2\pi) \times [13.6d_0,\ 41.4d_0]$ are also treated as sponge regions. A time-averaged flow field obtained with a separate simulation is used as a reference flow field. Near the far boundaries, grid stretching similar to the methodology of Rai & Moin (1993) is used to accelerate the sponge layer method. We verify the computational method with experimental data for this problem in § 5.

In § 5, flow regions responsible for strong sound production are evaluated with the vortex sound theory developed by Howe (1975, 1980). The theory shows that when an acoustic oscillation occurs in an inviscid, isentropic but rotational flow, then instantaneous acoustic power P_{ac} is generated in a volume V, which is given by

$$P_{ac} = \int_V p_{ac} \mathrm{d}V, \quad p_{ac} \equiv -\rho_\infty (\boldsymbol{\omega} \times \boldsymbol{u}) \cdot \boldsymbol{u}_{ac}, \tag{4.3}$$

where p_{ac} is instantaneous acoustic power per unit volume, $\boldsymbol{u}$ is the instantaneous fluid velocity, $\omega = \nabla \times \boldsymbol{u}$ is the vorticity, $\boldsymbol{u}_{ac}$ is the acoustic particle velocity, and ρ_∞ is the mean density of the fluid. The procedures to evaluate instantaneous acoustic power P_{ac} are described in Appendix B of Matsuura & Nakano (2012). We solve the Poisson equation of the velocity potential ϕ, i.e. (B.3) of Matsuura & Nakano (2012), in a domain with the same shape as the grid mentioned above, except that far boundaries in the r and z directions are trimmed to $r = 5.35d_0$ and $z = 4.07d_0$. Here, we denote as G^1 the trimmed grid of 8.2M grid points. We use two additional grids, G^0, G^{-1}, to compute ϕ. The grid G^0 is generated from G^1 by thinning out basically every two grid lines in all the directions, and has approximately 1M grid points. The grid G^{-1} has approximately 0.14M grid points and is generated from G^0 by thinning out similarly. We finally obtain ϕ and P_{ac} on G^0. To accelerate solving the Poisson equation on G^0, the same equation is iteratively solved first on G^{-1}, and its converged solution is used as an initial condition for solving ϕ iteratively on G^0. In this study, we consider P_{ac} generated in the following volume V:

$$V \equiv \{(r, \theta, z);\ (r, \theta, z) \in (V_1 \cup V_2 \cup V_3) \backslash V_4\} \tag{4.4}$$

where

$$V_1 \equiv [d_0/51,\ 4.93d_0] \times [0,\ 2\pi) \times [40\ \text{mm},\ 50\ \text{mm}], \tag{4.5}$$

$$V_2 \equiv [d_0/51,\ d_0/2] \times [0,\ 2\pi) \times [50\ \text{mm},\ 60\ \text{mm}], \tag{4.6}$$

$$V_3 \equiv [d_0/51,\ 4.93d_0] \times [0,\ 2\pi) \times [60\ \text{mm},\ 65\ \text{mm}], \tag{4.7}$$

$$V_4 \equiv (r_i,\ r_e) \times [0,\ 2\pi) \times (50 - h\ \text{mm},\ 50\ \text{mm}]. \tag{4.8}$$

A time-averaged flow field is necessary for evaluating $\boldsymbol{u}_{ac}$. In this study, we use the flow field averaged both for $9.46L_{im}/u_\infty$ and in the θ direction. The adequacy of the average time length is confirmed by comparing the flow field with that averaged for $15.1\,L_{im}/u_\infty$ in terms of the velocity profiles around jet shear layers.

5. Computational results

5.1. *Evolution of flow quantities from the initial condition to an equilibrium state under the passive control*

Following the discussion about the effective region in figure 5(*a*) at the end of § 3.4, an intermediate value of W/L_{im}, e.g. 0.2, is typical for the obstacle effects. We therefore select type D with $L_{im} = 50$ mm, which realizes $W/L_{im} = 0.2$, for the analysis. We choose h to be 5 mm because the results become almost invariant when $h \geqslant 3$ mm for this type. As found from figures 3(*c*) and 11(*d*), the measured data of the selected case exhibit tone suppression with turbulent backflows and the emergence of a new peak at $f_0/2$, which are key features observed in common for the effective cases. In this regard, the selected case is considered a representative one for investigating the effective cases, i.e. the effective region in figure 5(*a*).

As mentioned in § 4, we started our computation by attaching the obstacle on the end plate abruptly in a developed flow field of the baseline hole tone. Because measurements are conducted sufficiently long after the obstacle is attached on the end plate, we first discuss the computational results of a fully developed stage. For this purpose we here identify a stage where flows are in equilibrium by considering the time evolution of flow quantities from the initial condition. Although the flow fields are turbulent and three-dimensional because of the obstacle, the relationships among mass flow rates through the end plate hole, the radial velocities and streamwise velocities may be explained by an axisymmetric model in an average sense, which is also inferred from the existence of the most dominant peak at $f_0/2$ in the SP spectrum. Circumferentially averaged u_r and u_z are denoted $\langle u_r \rangle_\theta$ and $\langle u_z \rangle_\theta$, respectively.

Figure 13 compares the time histories of the non-dimensional mass flow rates through the end plate hole $\dot{m}_h^\dagger$, the circumferentially averaged radial velocities $\langle u_r \rangle_\theta$ near the hole inlet $(r, z) = (25.5 \text{ mm}, 49.5 \text{ mm})$, the circumferentially averaged streamwise velocities $\langle u_z \rangle_\theta$ at the hole inlet $(r, z) = (25.2 \text{ mm}, 50.5 \text{ mm})$, and the number of circumferential grid points among $j_{max} = 97$ points, i.e. the histogram, at $(r, z) = (25.5 \text{ mm}, 49.5 \text{ mm})$ and an instantaneous time t where pressure fluctuation $\Delta p = p - p_\infty (p_\infty = 101,325 \text{ Pa})$ belongs to an interval $(-80 + 4(m-1), -80 + 4m]$ characterized by $m \in \{1, \ldots, 40\}$, i.e.

$$N_m(t) = \#\{j \mid -80 + 4(m-1) < \Delta p_j(t) \leqslant -80 + 4m,\ 1 \leqslant j \leqslant 97\}, \quad m = 1, \ldots, 40. \tag{5.1}$$

Non-dimensional mass flow rate $\dot{m}_h^\dagger$ is defined by

$$\dot{m}_h^\dagger \equiv \frac{\dot{m}_h}{\pi (d_0/2)^2 \rho_\infty u_0}, \tag{5.2}$$

and the mass flow rates $\dot{m}_h$ are evaluated as

$$\dot{m}_h \equiv \int_\Omega \rho u_z r \mathrm{d}r\mathrm{d}\theta, \quad \Omega \equiv \{(r, \theta);\ (r, \theta) \in [0, d_0/2] \times [0, 2\pi)\}. \tag{5.3a,b}$$

The abscissa t^* is the time non-dimensionalized by L_{im} and c_∞: $t^* = 0$ corresponds to the initial condition, i.e. the time when the obstacle is attached abruptly to the end plate in the flow field of the baseline hole tone determined previously. In the figure, time histories for $t^* = 259$–854 are omitted.

In figure 13, there are three stages of flow states. Stage A is a time period where baseline hole tone oscillations still remain. Except for strong pressure propagation

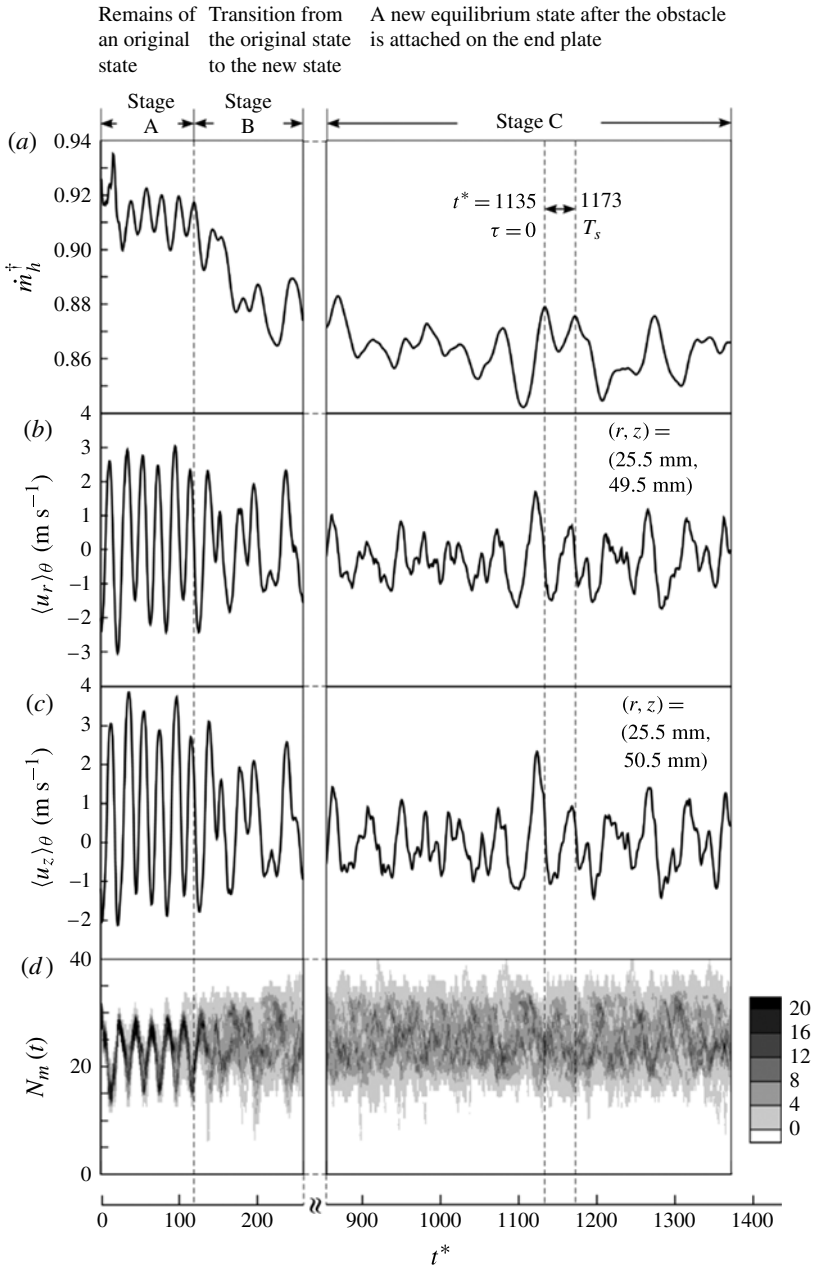

FIGURE 13. Comparisons of (*a*) the time histories of mass flow rates through the end plate hole $\dot{m}_h^\dagger$, (*b*) circumferentially averaged radial velocities $\langle u_r \rangle_\theta$ at the inlet of the hole, (*c*) cumferentially averaged streamwise velocities $\langle u_z \rangle_\theta$ at the inlet of the hole, (*d*) the number of circumferential grid points where pressure fluctuation belongs to the interval $N_m(t)$, $m = 1, 2, \ldots, 40$, defined by (5.1).

immediately after the obstacle is attached on the end plate, developed vortices in the jet shear layers do not change rapidly, and flow structures approaching the hole therefore do not change for a while in the stage. All the quantities are clearly sinusoidal until around $t^* = 120$, and become disordered thereafter, which means that

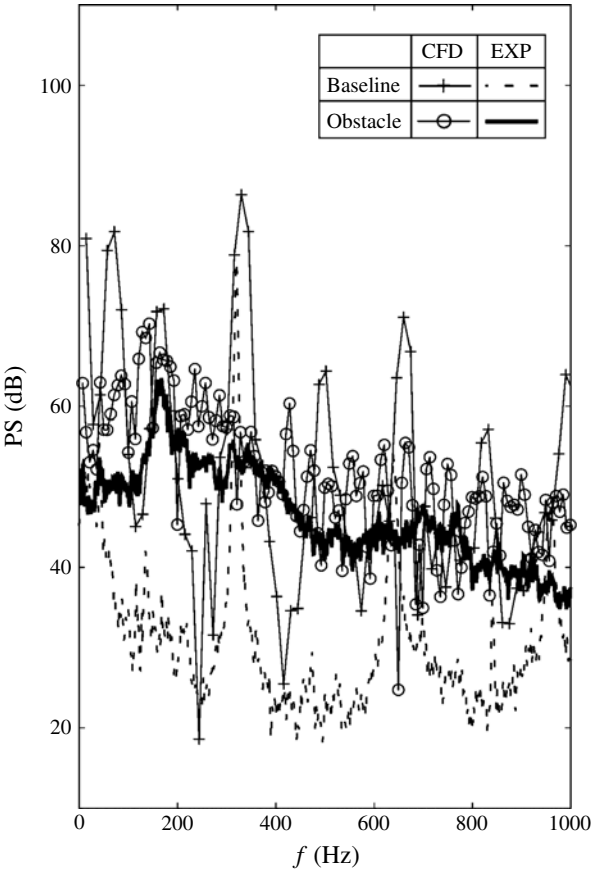

FIGURE 14. Comparisons of SP spectra between the computations and experiments both for the baseline and obstacle cases when $u_0 = 10$ m s^{-1} and $L_{im} = 50$ mm at $(r, z) = (1.80d_0, L_{im}/2)$. Type D with $h = 5$ mm is used in the obstacle case. The results for the baseline case are reproduced from Matsuura & Nakano (2012).

there is deviation from the original state with the oscillation at a frequency f_0 due to the obstacle. Stage C is a time period where flow states reach a new equilibrium, and corresponds to the measurements. Turbulent oscillations without apparent regular variation, which are different from those in Stage A, are observed. As explained later in figure 17, the flow fields of the baseline hole tone with periodic vortex rings are broken and fine turbulent structures are generated in this stage. The periods of the dominant variation of $\dot{m}_h^{\dagger}$, u_r and u_z become longer than those in Stage A except for small and rapid variation on the long and slow variation. The long and slow variation results from interaction between large recirculation regions formed near the obstacle corner and the main jet, which is mentioned later regarding figure 16. Stage B is the intermediate time period between Stages A and C.

5.2. *Validation of computation for the new equilibrium state*

Here, we examine the validity of the present computations by comparing SP spectra and qualitative behaviour of backflows between the computations and experiments.

First, figure 14 compares SP spectra between the computations and experiments when $u_0 = 10$ m s^{-1}. The comparisons are made for two cases: the baseline hole

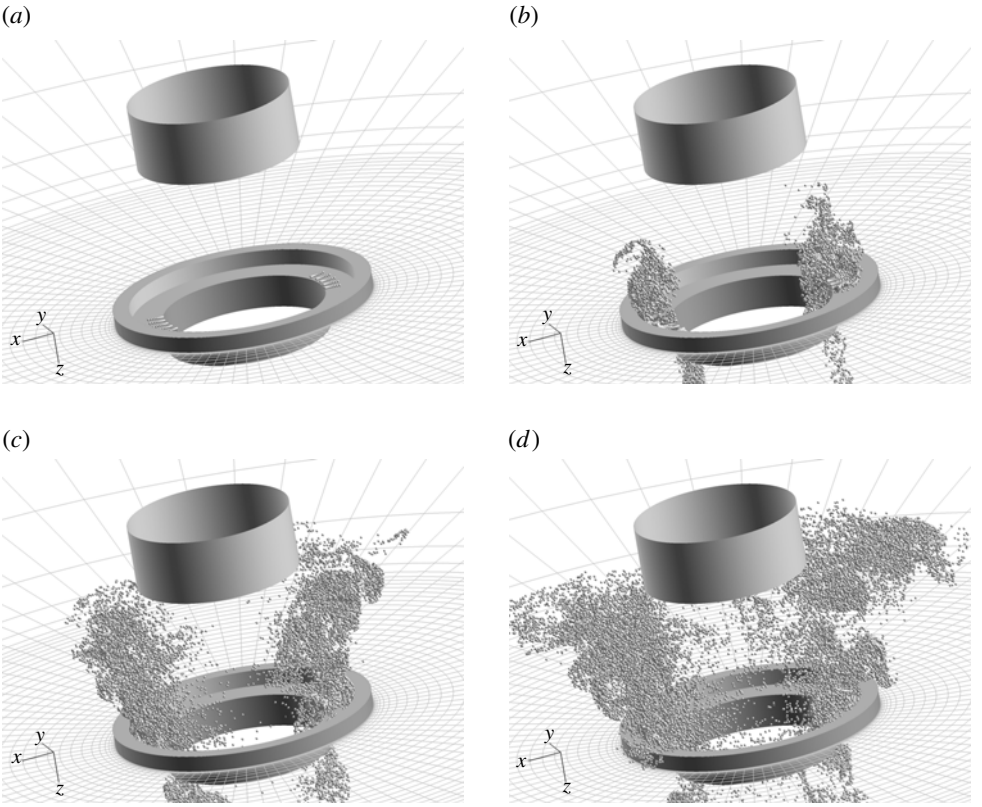

FIGURE 15. Behaviour of massless particles seeded from the neighbourhood of the end plate hole edge (type D with $h = 5$ mm, $L_{im} = 50$ mm): (*a*) $t^* = 855$, (*b*) $t^* = 912$, (*c*) $t^* = 1028$, (*d*) $t^* = 1143$.

tone, and the obstacle case of type D with $h = 5$ mm when $L_{im} = 50$ mm. To estimate the SP spectra in the computations, we use the time series data of pressure variation at $(r, z) = (1.80d_0, L_{im}/2)$ during the time periods of $478\,L_{im}/c_\infty$ and $962\,L_{im}/c_\infty$ for the baseline and obstacle cases, respectively. For the latter case the time series data are collected for $t^* = 446$–1408 which is well after Stage B. Regarding the experiments, the SP spectrum has a narrowband distribution in the baseline case and the most dominant peak corresponds to the frequency of the baseline hole tone. In the obstacle case, the original peak disappears completely and the SP spectrum becomes broadband. Meanwhile, a new peak lower than the original peak emerges around $f_0/2$. The present computations successfully predict the narrowband distribution for the baseline case, the broadband distribution without the original peak and the emergence of the low peak around $f_0/2$ in the obstacle case from a qualitative viewpoint. For the baseline case, the most dominant peak frequency and sound level of the hole tone are 330 Hz and 86.3 dB in the computation and 320 Hz and 78.1 dB in the experiment. For the obstacle case, these values are 143 Hz and 70.2 dB in the computation and 167.5 Hz and 63.5 dB in the experiment. Our computations for both cases also reasonably predict the frequencies and PS obtained by experiments from a quantitative viewpoint.

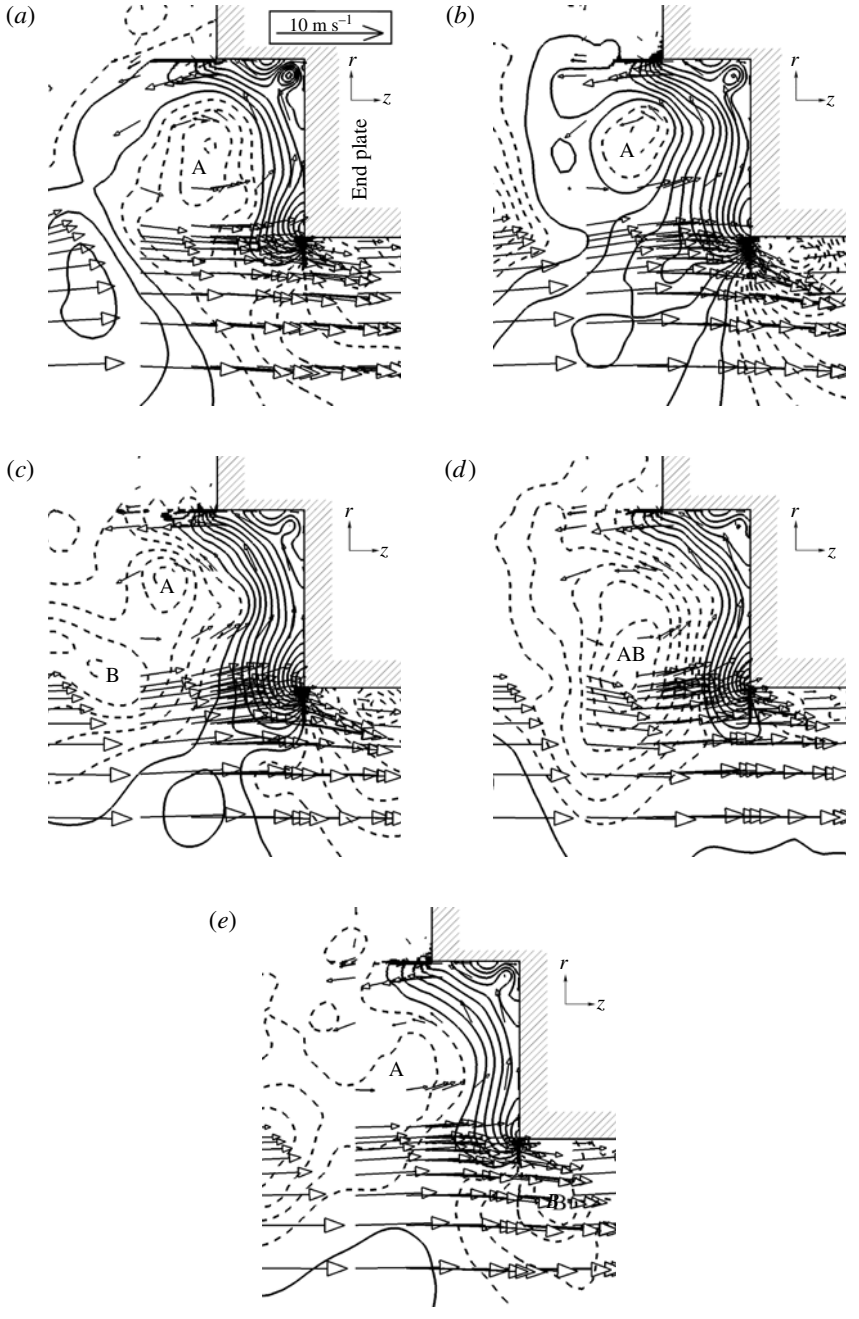

FIGURE 16. Time variation of circumferentially averaged pressure fluctuation (contours) and velocity fields (arrows) near the obstacle due to shear layer impingement on the hole edge for type D with $h = 5$ mm when $L_{im} = 50$ mm. The contours lines are drawn with 32 levels in the range [−30 Pa, 30 Pa]. Solid lines: positive region, dashed lines: negative region. (*a*) $t^* = 1135$ $(\tau = 0)$, (*b*) $t^* = 1143$ $(\tau = T_s/4)$, (*c*) $t^* = 1152$ $(\tau = 2T_s/4)$, (*d*) $t^* = 1163$ $(\tau = 3T_s/4)$, (*e*) $t^* = 1173$ $(\tau = 4T_s/4)$.

One might think that the above frequency difference of 24.5 Hz for the obstacle case is too big to be considered an agreement between the computation and experiment. As found from figure 4(*b*,*c*), flow structures do not change qualitatively. Based on eight and 15 previous samples for $u_0 = 8$ and 10 m s^{-1}, respectively, the ensemble averages of the most dominant peak frequencies are 124.4 and 161.3 Hz for $u_0 = 8$ and 10 m s^{-1}, respectively. The interpolated frequency at $u_0 = 9.5$ m s^{-1}, which is about the lowest value we regard as 10 m s^{-1} as mentioned previously in § 2, is 152.0 Hz. If we subtract 10 Hz, which is moderate uncertainty, from the above frequency, the final value becomes 142.0 Hz. Therefore, the peak frequency 143 Hz obtained by the computation makes sense. One might also think the sound levels are too different between the computation and experiment. However, we consider the observed differences between them to be quite natural. For the obstacle case, e.g., 70 and 63 dB correspond to 0.0632 and 0.0282 Pa, respectively. The present computation is based on a fully compressible methodology and handles absolute pressure, which means that we are discussing the 8th digit from the leading one. In addition to the experimental uncertainties mentioned in § 2, the direct sound computation is nothing but an approximation. Therefore, agreement between the computation and experiment is quite successful.

According to the above discussion, the present computation well reproduces the change from the original state to the new equilibrium state under passive control.

Secondly, we show that, in the present computation, highly turbulent backflows are ejected from the inner side of the obstacle, which is a key flow feature when the baseline hole tone is successfully suppressed, as explained in § 3.4 related to figure 5(*a*). Figure 15 shows the behaviour of massless particles seeded from two regions Ω_1 and Ω_2 near the hole during $t^* = 855$–1143. Here, Ω_1 and Ω_2 are defined respectively as

$$\Omega_1 \equiv \left\{(r, \theta, z);\ 26.3\ \text{mm} \leqslant r \leqslant 30.1\ \text{mm},\ -\frac{\pi}{12} \leqslant \theta \leqslant \frac{\pi}{12},\ z = 49.1\ \text{mm}\right\}, \quad (5.4)$$

$$\Omega_2 \equiv \left\{(r, \theta, z);\ 26.3\ \text{mm} \leqslant r \leqslant 30.1\ \text{mm},\ \tfrac{11}{12}\pi \leqslant \theta \leqslant \tfrac{13}{12}\pi,\ z = 49.1\ \text{mm}\right\}. \quad (5.5)$$

Some particles radially proceeding along the end plate near the hole are blocked by the obstacle and proceed upstream as backflows outside of the main jet, as shown later in detail in figure 16. Eventually they reach the nozzle exit. Some particles are incorporated in the main jet, and others disperse in the radial direction along the nozzle exit plane. The highly turbulent backflows disturb the shear layers of the main jet from the immediate neighborhood of the nozzle exit, and prevent the formation and growth of clearly organized vortices in the shear layers leading to the disorganization of a feedback loop of the baseline hole tone as mentioned below in § 5.3. Because the components of the present system, i.e. the nozzle, hole and obstacle, are axisymmetric, it might be thought that nearly axisymmetric flow structures develop under passive control, similar to the case for the baseline hole tone. However, because asymmetry grows rapidly after the impingement of the vortex rings on the end plate as shown below in figure 17(*a*), backflows from the obstacle are turbulent and asymmetric.

Figure 16 shows the time variation of pressure fluctuation Δp and velocity fields near the obstacle during $t^* = 1135$–1173, which is considered to be a typical period corresponding to the frequency of approximately $f_0/2$. The selected period is shown in figure 13 and corresponds to $1/T_s \sim f_0/2 \sim 176$ Hz. The flow fields are circumferentially averaged, and regions of $\Delta p \geqslant 0$ are shown by solid lines and those of $\Delta p < 0$ are shown by dashed lines. As seen in figure 16(*a*,*b*), stable and large

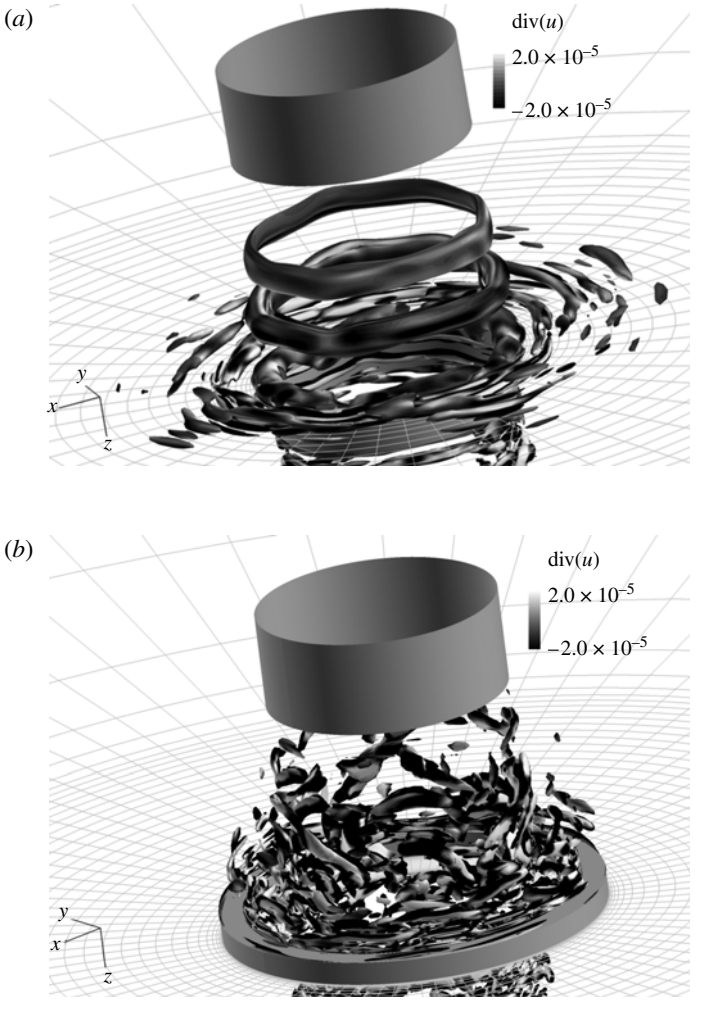

FIGURE 17. Comparison of vortical structures between (*a*) the baseline case (Matsuura & Nakano 2012) and (*b*) the obstacle case (type D with $h = 5$ mm). Vortices are visualized by the isosurfaces of the second invariant of the velocity gradient tensor $\boldsymbol{Q}^{\dagger} = 14.5$ (the baseline case) and 58 (the obstacle case) when $u_0 = 10$ m s^{-1} and $L_{im} = 50$ mm.

recirculation regions, marked 'A', exist near the obstacle corner at $\tau = 0$ and $T_s/4$. At these times, u_r at $(r, z) = (25.5$ mm, 49.5 mm) is decreasing as seen in figure 13, owing to the velocity distribution in the shear layer of the main jet. At $\tau = 2T_s/4$ (figure 16*c*), a low pressure region marked 'B' in the shear layer of the main jet approaches the hole edge. At $\tau = 3T_s/4$ (figure 16*d*), a pairing of 'A' and 'B' occurs and creates a large vortex marked 'AB'; u_r near $(r, z) = (25.5$ mm, 49.5 mm) then becomes positive, and much fluid, which is converted to backflows, enters the corner. At $\tau = 4T_s/4$ (figure 16*e*), the low pressure region 'B' separates from the large vortex 'AB' and enters the hole, which makes the flow field similar to that at $\tau = 0$. The existence of the corner vortex is consistent with the experimental observation mentioned in § 3.4. From the results, we may safely state that our computations correctly reproduce the physics of the present passive control of the hole tone.

5.3. *Continuous disorganization of vortex structures by an obstacle*

Figure 17 compares vortical structures of the baseline case and obstacle case D. The vortices are visualized by the isosurfaces of the second invariant of the velocity gradient tensor $\boldsymbol{Q}^\dagger = 14.5$ for the baseline case (Matsuura & Nakano 2012) and 58 for the obstacle case. Here, $\boldsymbol{Q}^\dagger$ is defined as

$$\boldsymbol{Q}^\dagger = \tfrac{1}{2}(-S_{ij}^\dagger S_{ji}^\dagger + \Omega_{ij}^\dagger \Omega_{ij}^\dagger), \tag{5.6}$$

where $S_{ij}^\dagger$ is the rate of strain tensor and $\Omega_{ij}^\dagger$ is the vorticity tensor. Here $\boldsymbol{Q}^\dagger$, $S_{ij}^\dagger$, $\Omega_{ij}^\dagger$ are non-dimensionalized by u_0 and L_{im}. In the baseline case, vortex rings are formed in the jet shear layers with the streamwise period corresponding to f_0. However, axisymmetric uniformity, which is responsible for f_0 in the baseline case, is apparently lost in the obstacle case, large-scale vortices disappear and fully three-dimensional vortices are generated from the immediate neighbourhood of the nozzle exit. The highly turbulent flows are maintained by the recirculation that results when the three-dimensional vortices in the jet shear layers convect downstream, interact with the obstacle and recursively disturb the jet flow from the nozzle exit by the backflows shown in figure 15.

Figure 18 shows space–time plots, i.e. the time evolution of the pressure fluctuation Δp distribution at $r = 4.7$, 20.2, 42.0 and 94.6 mm. Here, $r = 4.7$ mm corresponds to the neighbourhood of the centreline, $r = 20.2$ mm corresponds to the jet shear layer, and $r = 42.0$ and 94.6 mm correspond to the outside of the obstacle. First, we focus on Stage A. The space–time distribution in this stage is explained in detail in § 4.2 of Matsuura & Nakano (2012). At $r = 4.7$ mm, high and low pressure regions appear periodically in time, which corresponds to periodic propagation of pressure waves. The upstream and downstream sides of the end plate hole have opposite sign of the pressure as explained in the axisymmetric throttling mechanism (Matsuura & Nakano 2012). At $r = 20.2$ mm, a similar periodic pressure distribution appears close to the nozzle exit, which means that the region near the nozzle exit at this radial position corresponds to the inside of the jet, and the growth of the vortices in the shear layer is negligible. Outside the region, high and low pressure regions extend to the upper right, which means that shear layer vortices develop and convect downstream. At $r = 42.0$ and 94.6 mm, time-periodic high and low pressure regions uniform in the z direction appear upstream and downstream of the end plate. In Stage C, pressure variation is disorganized at $r = 4.7$ mm. At $r = 20.2$ mm high and low pressure regions extending to the upper right start from the immediate neighbourhood of the nozzle exit, which means that vortices convect downstream from the immediate neighbourhood of the nozzle exit, where the influence of regularly passing pressure waves is much more dominant in the baseline case than the influence of vortices. The vortex convection matches with the computational observation of incorporation of massless particles in the main jet mentioned in § 5.2. At $r = 42.0$ mm, apparent periodicity is lost and the magnitude of the pressure variation is also reduced.

As mentioned above, turbulent backflows from the inner side of the obstacle affect the shear layer growth of the main jet, and disorganize the shear layer. To show the magnitude of disturbances affecting the nozzle exit, the time histories of u_r, u_z and Δp near the nozzle exit, i.e. $(r, z) = (25.5\text{ mm}, 0.493\text{ mm})$, are shown in figure 19. In the baseline case, the typical differences between the maximum and minimum are 0.015 m s^{-1}, 0.019 m s^{-1} and 7.28 Pa for u_r, u_z and Δp, respectively within the time range shown in figure 17 of Matsuura & Nakano (2012). However, in the obstacle case, the differences between the maximum and minimum within $t^* = 854.6$–1372.3

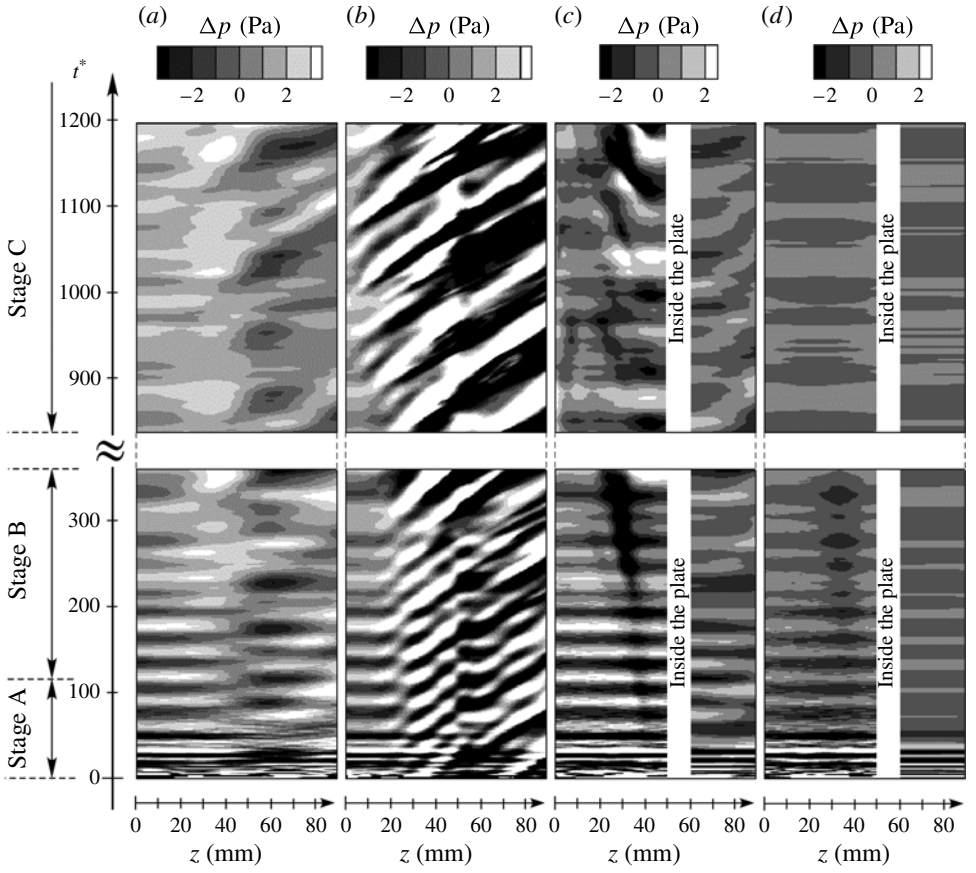

FIGURE 18. Space–time plots of pressure fluctuation Δp at: (*a*) $r = 4.7$ mm (near the centreline); (*b*) $r = 20.2$ mm (near the shear layer of the main jet); (*c*) $r = 42.0$ mm (outside of the obstacle, close to the centreline); (*d*) $r = 94.6$ mm (outside of the obstacle, far from the centreline). $z = 0$: nozzle exit.

are 1.18 m s^{-1}, 1.22 m s^{-1} and 5.43 Pa, which are two orders of magnitude larger for u_r and u_z, and the same magnitude for Δp. Therefore, much larger disturbances affect the nozzle exit in the obstacle case than in the baseline case.

To show that the present strategy of disorganizing the feedback loop by the obstacle leads to tone suppression, we study the effect of the obstacle on instantaneous acoustic power using the vortex sound theory developed by Howe (1975, 1980). P_{ac} is defined as the volume integral of p_{ac}, and P_{ac} therefore becomes large only when large p_{ac} ranges widely in the integration volume V as found from (4.3). For the present purpose, we analyse the period of approximately $f_0/2$ which is selected in § 5.2 for the obstacle case and compare the results with those of the baseline case. P_{ac} is evaluated at $t = nT_f/6$ $(n = 0, 1, \ldots, 6)$ and $t = nT_s/6$ $(n = 0, 1, \ldots, 6)$ for the baseline and obstacle cases, respectively. Figure 20 shows the spatial contribution $\langle p_{ac}\rangle_\theta$ to P_{ac} around the hole at $t = T_f/6$ and $2T_f/6$ in the baseline case and at $t = 2T_s/6$ and $3T_s/6$ in the obstacle case. The selected times correspond to the times when P_{ac} becomes maximal. Here, $\langle p_{ac}\rangle_\theta$ is defined as the average of p_{ac} in the θ direction. In the baseline case, two high $\langle p_{ac}\rangle_\theta$ regions are observed, which was

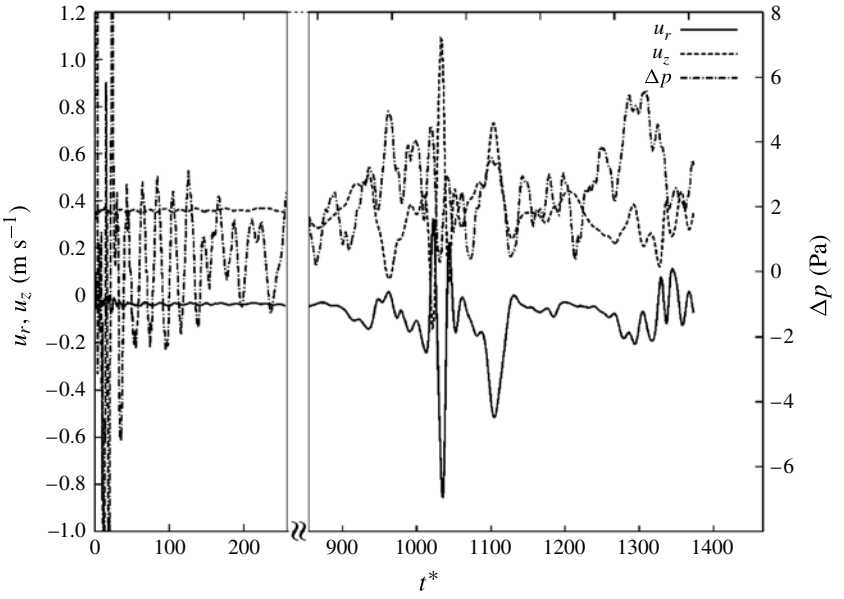

FIGURE 19. Time histories of u_r, u_z and Δp at $(r, z) = (25.5\ \text{mm}, 0.493\ \text{mm})$.

mentioned previously in the introduction. The highest $\langle p_{ac}\rangle_\theta$ region coincides with the outer edge of the separation region, and the second highest $\langle p_{ac}\rangle_\theta$ region is just on the upstream side of the end plate near the hole edge. On the other hand, in the obstacle case, high $\langle p_{ac}\rangle_\theta$ regions are observed only near the upstream edge inside the hole, which corresponds to the outer edge of a separation region also in this case as shown by $\langle u_z\rangle_\theta < 0$ in figure 13. Compared with the baseline case, the extent of high $\langle p_{ac}\rangle_\theta$ regions is much reduced and localized in the obstacle case corresponding to the appearance of the fine vortical structures mentioned above. Because P_{ac} is an integrated value it is much reduced in the obstacle case.

When we take into consideration the fact that high $\langle p_{ac}\rangle_\theta$ regions are observed near the upstream edge inside the hole both in the baseline and obstacle cases, it is concluded that P_{ac} integrated around the region mainly contributes to the discrete, i.e. f_0 and/or $f_0/2$ peak, tones. So, the reduction in P_{ac} mentioned above corresponds to the elimination of the f_0 peak in the obstacle case.

5.4. *Transition from the state of the baseline hole tone to the suppressed state*

So far, we have exclusively focused on the equilibrium state, i.e. Stage C, where the baseline hole tone phenomena are continuously suppressed by the obstacle. Although the evidently organized structures observed in the baseline case disappear in the obstacle case, a weak feedback loop is sustained even in the disorganized state as inferred from the maximum peak at $f_0/2$ in figure 14. In this subsection, we explain the initial emergence of the subharmonic frequency in the transient stage, i.e. Stage B. The origin of the subharmonic frequency is not obvious from the equilibrium state because memory of the transient process is lost in the state and the flow structures of the frequency develop as the result of the stability of the jet.

The baseline flow that we use as the initial condition in the present computation already involves acoustic back-reaction, which means that the acoustic motion

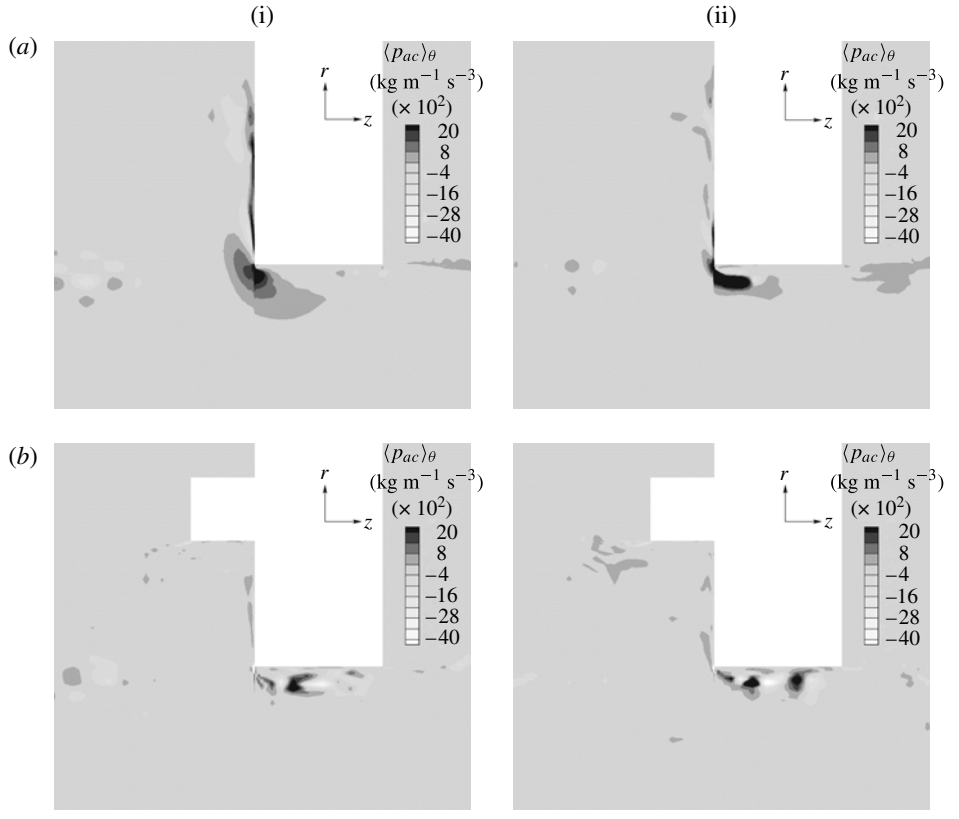

FIGURE 20. Spatial contribution $\langle p_{ac}\rangle_\theta$ to P_{ac} around the hole when $u_0 = 10$ mm and $L_{im} = 50$ mm. (*a*) Baseline case (Matsuura & Nakano 2012): (i) $t = T_f/6$, (ii) $t = 2T_f/6$. (*b*) Obstacle case (type D with $h = 5$ mm): (i) $t = 2T_s/6$, (ii) $t = 3T_s/6$.

determines the flow features. In principle the flow could develop in a very different way in the absence of the acoustic back-reaction with the obstacle. So, the transition, i.e. Stage B, might be thought to be just an artifact of the numerical procedure. However, acoustic motion is very fast when compared to the characteristic speed of the backflow generated in the presence of the obstacle. Therefore, this fact justifies the present computation in which the initial state can develop as in the baseline case and then be disorganized as the backflow contaminates the initial shear layer.

Figure 21 shows the time variation of pressure fluctuation Δp and velocity fields at $\theta = 0$ rad for $t^* = 100$–180. During $t^* = 100$–120 organized vortices periodically aligned in the jet shear layers impinge on the hole edge. Recirculation near the interior corner of the obstacle is immature because no regions of very low pressure are observed. During $t^* = 130$–140 a vortex in the jet shear layer enters the corner region. When the recirculation region near the corner develops and becomes strong, it begins to interact with the shear layers of the main jet, and the corner vortex begins to deform the shear layers around the hole edge as seen from the interaction of the vortices marked 'A' and 'B' in figure 21(*e*,*f*). Eventually, there is a vortex pairing as seen from the pairing of vortices A and C in figure 21(*g*–*i*). It is well established that a vortex pairing produces a subharmonic frequency (Ho & Huerre 1984). According to our past studies (Matsuura & Nakano 2012) and figure 13, the variation in mass

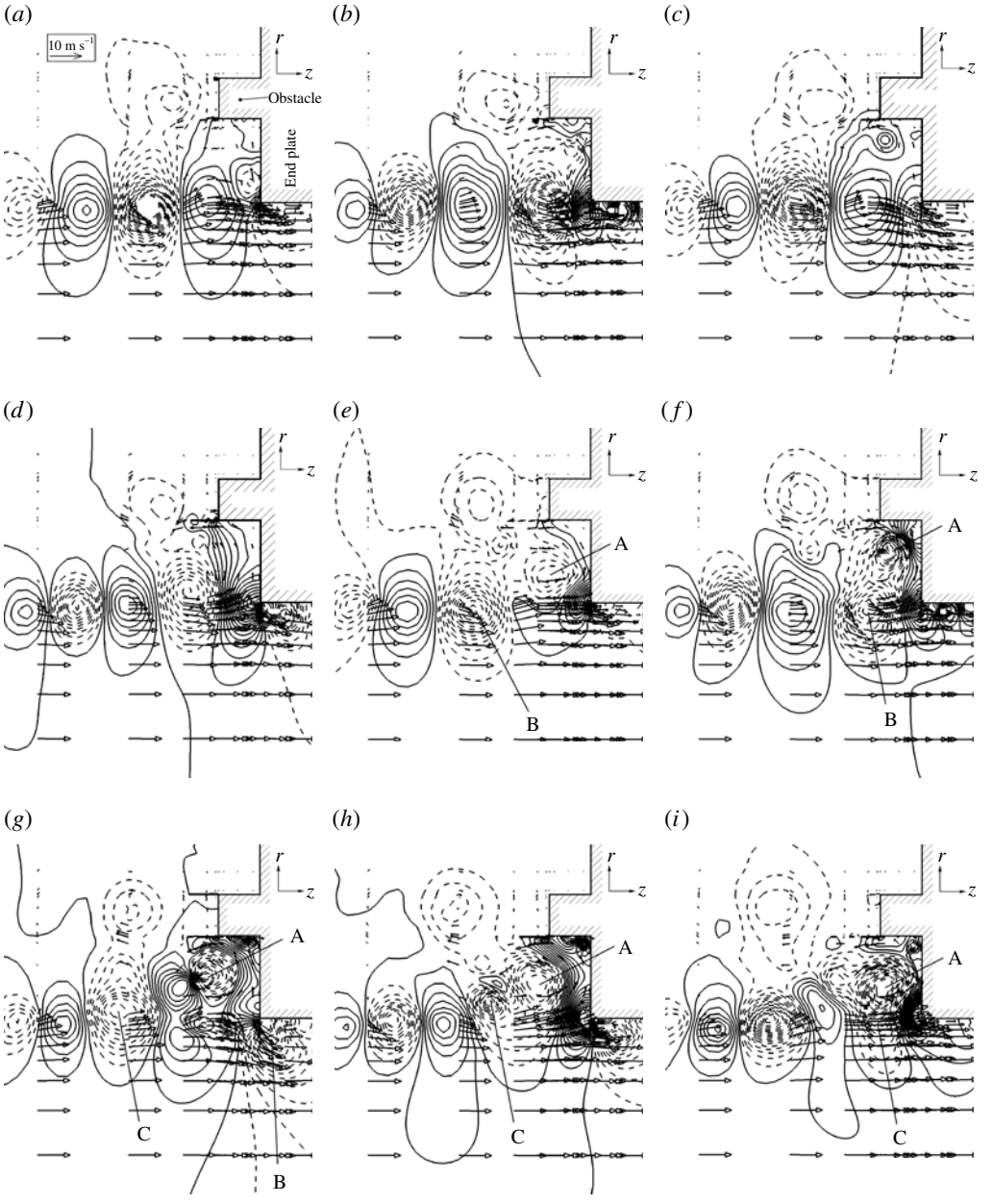

FIGURE 21. Time variation in pressure fluctuation Δp and velocity fields at $\theta = 0$ rad during the transition from the state of the baseline hole tone to the suppressed state for obstacle type D with $h = 5$ mm when $u_0 = 10$ mm and $L_{im} = 50$ mm; the contours lines are drawn with 32 levels in the range [−30 Pa, 30 Pa]; solid lines: positive region, dashed lines: negative region. (*a*) $t^* = 100$, (*b*) $t^* = 110$, (*c*) $t^* = 120$, (*d*) $t^* = 130$, (*e*) $t^* = 140$, (*f*) $t^* = 150$, (*g*) $t^* = 161$, (*h*) $t^* = 171$, (*i*) $t^* = 180$.

flow rates through the hole and global pressure propagation correspond to vortex impingement on the hole edge. Therefore, the modulation of the shear layers of the main jet by the vortex pairing accordingly changes the mass flow rates through the

hole, velocity fields near the hole and pressure fluctuation as found in figure 13. As the result of the pairing, a large corner vortex, which is also confirmed from the empirical eigenfunctions shown later in figure 23, develops and continues to interact with the main jet thereafter as explained in § 5.2.

5.5. *Proper orthogonal decomposition analysis for dominant structures in the equilibrium state*

As mentioned previously, there is weak feedback with peak frequency of $f_0/2$ even in the disorganized state under equilibrium. Meanwhile, as found in § 5.3, the region of high contribution to P_{ac}, which is necessary for the feedback, is around the outer edge of the separated region near the hole edge, and is dominantly affected by the impinging vortices on the hole edge. In order to clarify the flow structure of the vortex impingement submerged in the disorganized flows, i.e. the fundamental flow structure that constitutes the stable states in which sound is continuously suppressed, we extract dominant unsteady behaviours, which are mutually independent, near the hole edge in the equilibrium state by a proper orthogonal decomposition (POD) analysis.

The method used in this study is Sirovich's snapshot POD method (Sirovich & Rodriguez 1987). By this method, the whole pressure fluctuation field on $\Omega_{all} \equiv \bigcup_{k=1}^{N_d} \Omega_k$ is orthogonally decomposed according to M instantaneous snapshots of the whole flow field. Here, $\Omega_k,\ k = 1, \ldots, N_d$ corresponds to each zone mentioned in § 4, and N_d is the total number of zones, i.e. $N_d = 7$. In the method, the fluctuation $p'(x, t) = p(x, t) - \overline{p(x)}$ is expanded by a set of eigenfunctions $\{\phi_i(x)\}_{i=1}^{M}$, which are also called 'modes', and the corresponding coefficients $\{a_i(x)\}_{i=1}^{M}$ as

$$p'(x, t) \sim p'_M(x, t) \equiv \sum_{i=1}^{M} a_i(t)\phi_i(x), \qquad (t, x) \in I \times \Omega_{all}. \tag{5.7}$$

Here, $\overline{p(x)}$ is the time-averaged pressure field; $\overline{p(x)}, p'(x, \cdot), p'_M(x, \cdot)$ and $\phi_i(x)$ are all N_{all}-dimensional vectors of positions with a single coordinate. I is a set of times when snapshots are sampled. N_{all} is the total number of grid points in Ω_{all}, i.e.

$$N_{all} \equiv \sum_{k=1}^{N_d} N_k. \tag{5.8}$$

Here, N_k is the number of grid points in Ω_k. Strictly speaking, there is a duplication of elements in $p'(x, \cdot)$ because $\exists i, j \in \{1, \ldots, N_d\}$ of $i \neq j$, $\Omega_i \cap \Omega_j \neq \phi$. However, the measures of $\Omega_i \cap \Omega_j$ for such i, j are very small compared with those of the zones, and the duplication is therefore considered to be negligible in these analyses. As discussed later on, the eigenfunctions $\{\phi_i(x)\}_{i=1}^{M}$ and the corresponding coefficients $\{a_i(x)\}_{i=1}^{M}$ are successfully evaluated by this treatment. Two cases are considered where the snapshots are collected every $6000\Delta t$ in case 1 and $9000\Delta t$ in case 2 to investigate the effect of the time resolution of data employed for the POD analysis on eigenvalues, eigenfunctions and POD mode coefficients. M is 240 in both cases.

In this study, we consider the top two modes. As the result of the analysis, the most dominant, i.e. first mode, occupies nearly 10 % of the total energy and the second dominant mode occupies 5–7 %. Figure 22 shows the time histories of the coefficients of the first and second POD modes in both cases, and circumferentially averaged pressure fluctuation Δp at $(r, z) = (25.5\ \text{mm}, 49.5\ \text{mm})$. Only slight shifts between

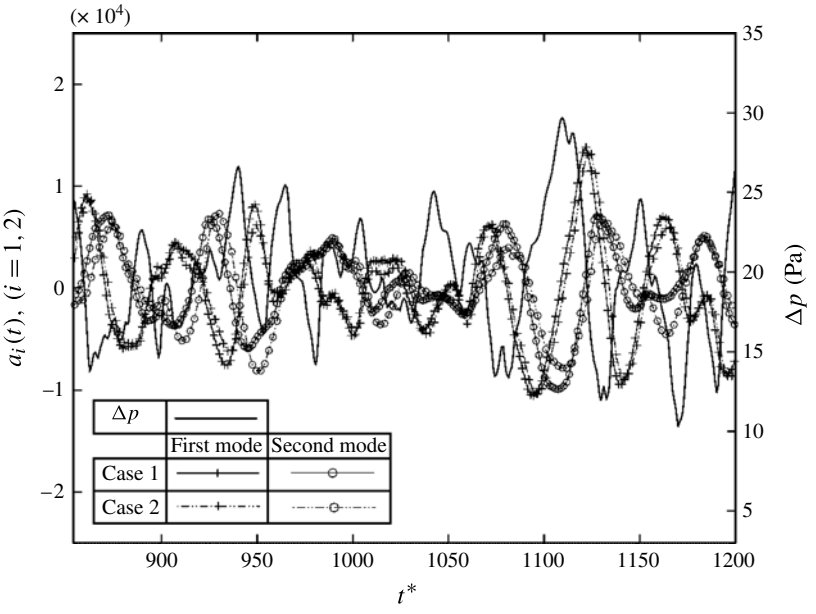

FIGURE 22. Time histories of the coefficients of the first and second POD modes, and circumferentially averaged pressure fluctuation Δp at $(r, z) = (25.5\text{ mm}, 49.5\text{ mm})$. Snapshots are collected every $6000\,\Delta t$ for case 1 and every $9000\,\Delta t$ for case 2. M is 240 for both cases.

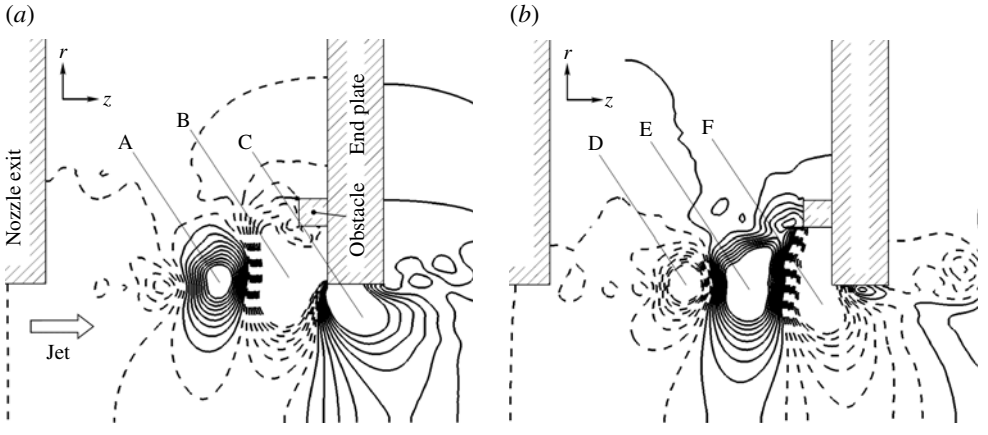

FIGURE 23. First and second empirical eigenfunctions (case 1). The contours lines are drawn with 17 levels in the range $[-0.0004, 0.0004]$. The eigenfunctions are circumferentially averaged. Solid lines: positive region, dashed lines: negative region. (*a*) First mode. (*b*) Second mode.

the cases are observed. Figure 23 shows the first and second empirical eigenfunctions in case 1. The eigenfunctions are circumferentially averaged. Although not shown here, we have confirmed that differences in the first and second eigenfunctions between cases 1 and 2 are negligible. Regarding the first mode, there are positive and negative regions 'A' and 'B' upstream of the end plate, and positive region 'C' inside the hole

in both cases. Regarding the second mode, there are negative, positive and negative regions 'D', 'E' and 'F' upstream of the end plate.

As in figure 17, axisymmetric vortical structures observed in the baseline case break up into fine eddies in the obstacle case. However, the convection of high and low pressure regions periodically aligned in the streamwise direction is still a dominant motion in the obstacle case. In figure 22, the phase of the coefficient of the first POD mode appears to be delayed by $\pi/2$ compared with Δp. The phase of the coefficient of the second POD mode is almost the opposite to Δp. There is order in the pressure distribution within each eigenfunction and the emergence of the eigenfunction when Δp is decomposed, which is common to the baseline hole tone discussed in § 5 of Matsuura & Nakano (2012). In their paper, the axisymmetric throttling mechanism linking mass flow rates through the hole, vortex impingement and global pressure propagation was proposed. The mass flow rate through the hole varies owing to a change in the direction of velocity vectors at the hole inlet because of the impingement of jet shear layers accompanying the variation in velocity vectors in the streamwise direction. At the same time, pressure waves are generated at the outer edge of the separation region near the upstream edge of the hole and on the upstream side of the end plate near the hole edge. When we take into account the eigenfunctions mentioned above, the spatial contribution $\langle p_{ac} \rangle_\theta$ to P_{ac} around the hole shown in figure 20 and the variation in the velocity vectors accompanying the variation in mass flow rates through the hole shown in figure 13, the axisymmetric throttling mechanism still holds even in the obstacle case.

6. Conclusions

We have investigated the disorganization of the feedback loop of the hole tone produced when a jet, issued from a circular nozzle or hole in a plate, goes through a similar hole in a downstream end plate. We proposed a new passive control method for suppressing the tone with an axisymmetric obstacle on the end plate. We found that the effect of the obstacle is well described by the combination $(W/L_{im}, h)$ where W is the distance from the edge of the end plate hole to the inner wall of the obstacle, L_{im} is the impingement length and h is the height of the obstacle. The effective region has a tongue-like shape with the effective point of minimum $h \sim 2.5$ mm around $W/L_{im} = 0.2$. The experiments showed that common features in the cases where the hole tone is successfully suppressed are turbulent backflows that are ejected from the inner side of the obstacle and the emergence of a new peak at the subharmonic frequency of the baseline hole tone. We performed a direct sound computation for the obstacle with inner diameter of 35.5 mm and $h = 5$ mm, where axisymmetric uniformity observed in the baseline case is broken almost completely in the obstacle case. The destruction of the original large-scale vortices and the disorganization of the feedback loop are maintained by the process in which three-dimensional vortices in the jet shear layers convect downstream, interact with the obstacle and recursively disturb the jet flow from the nozzle exit, which prevents the formation and growth of clearly organized vortices in the shear layer of the main jet. We studied the effect of the obstacle on the instantaneous acoustic power using Howe's vortex sound theory. While regions near the upstream edge inside the end plate hole, which is the largest sound source for the peak tone of the baseline, are responsible for producing sound also in the obstacle case, the acoustic power is much lower than that in the baseline case owing to the disorganized state. The emergence of the new peak at the subharmonic frequency was shown to begin as the result of pairing between the

vortices in the shear layer of the main jet and the corner vortices. By integrating the results of the snapshot POD, Howe's vortex sound theory, time histories of mass flow rates through the end plate and the radial and streamwise velocities at the inlet of the hole, it was shown that the axisymmetric throttling mechanism still holds even in the obstacle case.

Acknowledgements

This research was supported both by the Global COE Program 'World Center for Education and Research for Trans-disciplinary Flow Dynamics', of Tohoku University and by the Collaborative Research Project of the Institute of Fluid Science, Tohoku University. Computational resources were provided by the Advanced Fluid Information Research Center of the Institute of Fluid Science, Tohoku University.

REFERENCES

BLAKE, W. K. 1986 *Mechanics of Flow-Induced Sound and Vibration,* Vol. 1. Academic.

CATTAFESTA, L., WILLIAMS, D., ROWLEY, C. & ALVI, F. 2003 Review of active control of flow-induced cavity resonance. *AIAA Paper* 2003-3567.

CHANAUD, R. C. & POWELL, A. 1965 Some experiments concerning the hole and ring tone. *J. Acoust. Soc. Am.* **37** (5), 902–911.

FREUND, J. B. 1997 Proposed inflow/outflow boundary condition for direct computation of aerodynamic sound. *AIAA J.* **35** (4), 740–742.

GAD-EL-HAK, M. 2000 *Flow Control: Passive, Active and Reactive Flow Management*. Cambridge University Press.

GAITONDE, D. V. & VISBAL, M. R. 2000 Padé-type higher-order boundary filters for the Navier–Stokes equations. *AIAA J.* **38** (11), 2103–2112.

GINEVSKY, A. S., VLASOV, Y. V. & KARAVOSOV, R. K. 2010 *Acoustic Control of Turbulent Jets*. Springer.

HO, C.-M. & HUERRE, P. 1984 Perturbed free shear layers. *Annu. Rev. Fluid Mech.* **16**, 365–424.

HOWE, M. S. 1975 Contributions to the theory of aerodynamic sound, with application to excess jet noise and the theory of the flute. *J. Fluid Mech.* **71**, 625–673.

HOWE, M. S. 1980 The dissipation of sound at an edge. *J. Sound Vib.* **70** (3), 407–411.

HOWE, M. S. 1998 *Acoustics of Fluid-Structure Interactions*. Cambridge University Press.

IZAWA, S. 2011 Active and passive control of flow past a cavity. In *Wind Tunnels and Experimental Fluid Dynamics Research* (ed. J. C. Lerner & U. Boldes), pp. 369–394. InTech.

LANGTHJEM, M. A. & NAKANO, M. 2010 A three-dimensional study of the hole-tone feedback problem. *RIMS Kôkyûroku* **1697**, 80–94.

LELE, S. K. 1992 Compact finite difference schemes with spectral-like resolution. *J. Comput. Phys.* **103** (1), 16–42.

MATSUURA, K. & KATO, C. 2007 Large-eddy simulation of compressible transitional flows in a low-pressure turbine cascade. *AIAA J.* **45** (2), 442–457.

MATSUURA, K. & NAKANO, M. 2011 Direct computation of a hole-tone feedback system at very low Mach numbers. *J. Fluid Sci. Technol.* **6** (4), 548–561.

MATSUURA, K. & NAKANO, M. 2012 A throttling mechanism sustaining a hole tone feedback system at very low Mach numbers. *J. Fluid Mech.* **710**, 569–605.

MICHALKE, A. 1984 Survey on jet instability theory. *Prog. Aerosp.* **21**, 159–199.

RAI, M. M. & MOIN, P. 1993 Direct numerical simulation of transition and turbulence in a spatially evolving boundary layer. *J. Comput. Phys.* **109** (2), 169–192.

RAYLEIGH, LORD 1945 *Theory of Sound,* Vol. 2. Dover.

ROCKWELL, D. & NAUDASCHER, E. 1979 Self-sustained oscillations of impinging free shear layers. *Annu. Rev. Fluid Mech.* **11**, 67–94.

ROSSITER, J. E. 1962 The effect of cavities on the buffeting of aircraft. Royal Aircraft Establishment *Tech. Mem.* 754.

ROWLEY, C. W. & WILLIAMS, D. R. 2006 Dynamics and control of high-Reynolds-number flow over open cavities. *Annu. Rev. Fluid Mech.* **38**, 251–276.

SIROVICH, L. & RODRIGUEZ, J. D. 1987 Coherent structures and chaos: a model problem. *Phys. Lett.* A **120** (5), 211–214.

STUDENT, 1908 The probable error of a mean. *Biometrika* **6** (1), 1–25.